

Sky Subtraction in an Era of Low Surface Brightness Astronomy

Lee S. Kelvin,^{1,2,3} Imran Hasan² and J. Anthony Tyson²

¹*Department of Astrophysical Sciences, Princeton University, 4 Ivy Lane, Princeton, NJ 08544, USA*

²*Department of Physics, University of California, One Shields Ave., Davis, CA 95616, USA*

³*Astrophysics Research Institute, Liverpool John Moores University, IC2, LSP, 146 Brownlow Hill, Liverpool, L3 5RF, UK*

Accepted XXX. Received YYY; in original form ZZZ

ABSTRACT

The Vera C. Rubin Observatory Wide-Fast Deep (WFD) sky survey will reach unprecedented surface brightness depths over tens of thousands of square degrees. Surface brightness photometry has traditionally been a challenge. Current algorithms which combine object detection with sky estimation systematically over-subtract the sky, biasing surface brightness measurements at the faint end and destroying or severely compromising low surface brightness light. While it has recently been shown that properly accounting for undetected faint galaxies and the wings of brighter objects can in principle recover a more accurate sky estimate, this has not yet been demonstrated in practice. Obtaining a consistent spatially smooth underlying sky estimate is particularly challenging in the presence of representative distributions of bright and faint objects. In this paper we use simulations of crowded and uncrowded fields designed to mimic Hyper Suprime-Cam data to perform a series of tests on the accuracy of the recovered sky. Dependence on field density, galaxy type and limiting flux for detection are all considered. Several photometry packages are utilised: SOURCE EXTRACTOR, GNUASTRO, and the LSST SCIENCE PIPELINES. Each is configured in various modes, and their performance at extreme low surface brightness analysed. We find that the combination of the SOURCE EXTRACTOR software package with novel source model masking techniques consistently produce extremely faint output sky estimates, by up to an order of magnitude, as well as returning high fidelity output science catalogues.

Key words: techniques: image processing – methods: observational – surveys – galaxies: structure – galaxies: general – galaxies: fundamental parameters

1 INTRODUCTION

The human eye is unique in its capacity to look up at the night sky and easily separate out a wide variety of astronomical objects from the all encompassing celestial sphere upon which they lay. A computer, however, finds such a task decidedly non-trivial, often requiring extensive training, testing, and the use of a bespoke data processing pipeline. Tasks such as object detection, segmentation, point source estimation, and, crucially, sky estimation are all important components of many professional image processing pipelines. Deriving algorithms to accurately and rapidly perform such tasks has been an active area of research over the last several decades, with the issue becoming more pressing in recent years as we rapidly enter an era of big data astronomy which combines wide surveyed areas with unprecedented depth.

Contemporary astronomical observatories are located at sites with optimal seeing, photometric stability, and dark skies. Extremely dark ground-based sites with little to no light pollution are able to achieve sky brightness levels down to $\mu_V \sim 22$ mag arcsec⁻² (Garstang 1989). Without the impediment of an atmosphere, space-based facilities such

as the Hubble Space Telescope (HST) are able to probe $\sim 1 - 2$ mag arcsec⁻² deeper still (see, e.g., Knapen & Trujillo 2017, and references therein). Taking full advantage of such sites in combination with a careful observing strategy and a minimally aggressive sky subtraction technique now allows us to probe beyond the $\mu = 30$ mag arcsec⁻² threshold on an increasingly regular basis (Iodice et al. 2016; Trujillo & Fliri 2016). Such methodologies allow for formerly hidden galaxy structures to be seen and catalogued for the first time (e.g., Kelvin et al. 2018). The previously hidden low surface brightness (LSB) Universe continues to unveil a wealth of information across multiple scales, from LSB-type dwarfs (van Dokkum et al. 2015; Williams et al. 2016) to circumgalactic stellar haloes (D’Souza et al. 2014; Wang et al. 2019) and the mass-merging remnant intracluster light (Montes & Trujillo 2014, 2018, 2019).

Optimal observing conditions notwithstanding, non-signal features of any astronomical image must still be characterised to enable further scientific analyses. Such features typically consist of three primary components: the instrumental background produced by the observing hardware, such as CCD edge effects (Goldstein et al. 2015), scattered

arXiv:2301.05793v1 [astro-ph.IM] 14 Jan 2023

light from optics within the telescope (Karabal et al. 2017), and saturation features (Desai et al. 2016); the temporal background from terrestrial effects, such as zodiacal light, airglow and cosmic rays (Fixsen et al. 2000), and; the astrophysical background from sources which remain fixed in the sky, such as diffuse stellar light from bright sources and galactic cirrus. Additional contaminant flux such as satellite trails (Cheselka 1999; Vandame 2001; Storkey et al. 2004) must also be accounted for as part of the background estimation and handling process.

Many contemporary astronomy image reduction pipelines do not accurately preserve LSB flux, destroying this information at the sky subtraction phase. Furthermore, information on the undetected extragalactic background light (EBL), primarily due to fainter galaxies, is often not taken into account. Such pipelines tend to operate top-down: first detecting objects above a running biased initial sky estimate, then iteratively estimating object and sky fluxes. This produces good photometry at higher surface brightnesses, but is subject to sky bias due to very faint undetected galaxies. A complementary approach is to work bottom-up: first estimating sky, building a sky model, and only then detecting and measuring individual objects in a final step. The risk here is mistakenly assigning noise or contaminant flux to such sources, thereby overestimating their total flux. The potential for a bottom-up source detection algorithm to link several astrophysical sources together via a ‘flux-bridge’ is significant, for example, in densely packed regions of the sky, for observations whereby the source encompasses a large fraction of the detector field of view, or in regions whereby some other such flux contaminant is evident such as galactic cirrus. The key towards facilitating science at ultra low surface brightnesses is in producing accurate and robust sky estimations across a wide variety of potentially contaminated source flux.

The process begins with automated photometry and the detection of individual objects. This is a multi-step process which becomes more challenging at faint surface brightnesses. One of the first such software packages to address this task across a wide dynamic range and for faint galaxies was the Faint Object Classification and Analysis System (FOCAS) Jarvis & Tyson (1981). Using non-parametric statistical pattern recognition, it was initially driven by the need for surface photometry on faint co-added photographic plates, and later was extensively used on fainter CCD data. The output of a Bayesian detection algorithm with an optimal filter and adjustable detection threshold is fed to an area assembly stage, followed by spatial segmentation, iterative sky level estimation, object photometry, a hypersurface classifier, and output catalogue containing the segmentation history of each object. Recursive FOCAS runs on deep CCD data asymptotically, reaching completeness at the noise level. The program has many adjustable parameters: detection threshold, sky histogram, detection filter, segmentation sensitivity, intensity moments weighting kernel, and objects classification parameters.

A subsequent streamlined software package based upon similar operating principles, SOURCE EXTRACTOR (Bertin & Arnouts 1996, version 2.25.3 being used in this study), was developed for faster automated photometry. While based partly on similar precepts to that of FOCAS, it was designed to have a more global and computationally efficient

segmentation algorithm, necessarily trading some control over optimal filters in each phase that was present in FOCAS. The SOURCE EXTRACTOR package is capable of covering a wider range of object sizes however, and also outputs a sky estimation map and a detected source catalogue. For sky estimation, the local background around objects is clipped iteratively at $\pm 3\sigma$ around the sky median. Like a single-pass FOCAS, it produces a sky that is biased high. The SOURCE EXTRACTOR software package has been instrumental in the development of several image processing pipelines in recent years, notably the SIGMA (Kelvin et al. 2010, 2012) and GALAPAGOS (Barden et al. 2012; Hiemer et al. 2014) packages, both of which have been used to rapidly process and analyse millions of galaxies across multiple wavelengths using data from a wide variety of surveys. The SOURCE EXTRACTOR package itself has since been rewritten as SOURCE-EXTRACTOR++¹, incorporating a number of novel developments made in recent years. Furthermore, building upon the successes of SOURCE EXTRACTOR, a range of contemporary software packages which utilise similar operating processes have also become available, such as PROFOUND (Robotham et al. 2018) and MTOBJECTS (Teeninga et al. 2015).

More recently, the GNU ASTRONOMY UTILITIES (GNUASTRO; Akhlaghi & Ichikawa 2015; Akhlaghi 2019) software package (version 0.17 used here²) has been released, providing a suite of programs and functions for use in the manipulation of astronomical data. One such constituent program is NOISECHISEL, a program for the detection of faint, extended, nebulous astrophysical objects. NOISECHISEL relies on a non-parametric algorithm rather than any particular function or fitting technique to identify contiguous regions whose noise properties are altered by the underlying faint astrophysical objects buried beneath. Other signal processing algorithms, like those mentioned above, are biased towards detecting objects that are sufficiently similar to the detection kernel being used. As NOISECHISEL does not depend on knowing the shapes or profiles of sources beforehand, and does not require any a priori knowledge of the spatial properties of astrophysical objects, it is therefore unbiased in this regard. Counter to the top-down operating principles of many prior source detection software packages, NOISECHISEL operates on a bottom-up philosophy, attempting first to characterise the background noise in an image before classifying the residual signal flux. This approach has potential advantages in the detection and characterisation of LSB light, but also carries certain risks with regards the possible inclusion of noise in estimates of signal flux, as further discussed later in this study.

A modern detection algorithm is being developed for use with the Vera C. Rubin Observatory (hereafter, Rubin Observatory), formerly known as the Large Synoptic Survey Telescope, which will undertake a 10-year Wide-Fast Deep (WFD) survey of the southern sky called the Legacy Survey of Space and Time (LSST, Ivezić et al. 2019). A version of this software is currently used in the data reduction pipeline for the Hyper Suprime Cam Subaru Strategic Program (HSC-SSP; Aihara et al. 2018a,b; Bosch et al. 2018, 2019). This algorithm first identifies high signal-to-

¹ <https://sourceextractorplusplus.readthedocs.io>

² <http://www.gnu.org/software/gnuastro>

noise stars on the stellar locus, using these to model the spatially varying PSF over the entire image and subsequently facilitating characterisation of simply connected regions above a given detection threshold as detections (see Section 3.5.1 for further details). Detected sources are then masked, so a polynomial model can be fit to the remaining pixels to evaluate a sky background model. This process is repeated iteratively at the CCD level until a final PSF model, detection catalogue, and sky background model are achieved.

When reducing and analysing astronomical imaging data, it is often best to separate the two tasks of sky estimation and catalogue generation (e.g., object photometry; also see Akhlaghi 2019). A Bayesian statistical approach to sky estimation which uses the known faint galaxy counts has recently been pursued by Ji et al. (2018). It was shown in simulations that robust sky precision of ~ 4 ppm is in principle possible.

In this study, we explore a number of alternative background estimator configuration modes which have the potential to be more accurate and less impacted by the extended surface brightness profiles of galaxies and the density of the local image environment as compared to traditional techniques. The primary challenge to be addressed is the performance of these techniques over realistic large deep fields with a broad range of object densities and sizes. Building upon prior efforts in this field, we present a range of sky estimation configuration modes which are designed to accurately preserve sky flux over large fields in realistic deep imaging, paving the way for future LSB science cases. For a fully realistic approach, we apply these configuration modes to full image simulations based upon recent deep survey imaging, testing the robustness of sky estimation outputs and source photometry for each.

The remainder of this paper is structured as follows. Section 2 provides an overview of our simulated dataset using the GALSIM software package. Section 3 discusses all sky estimation software packages and distinct software configuration modes explored within this study. Results and discussion are presented in Section 4, and conclusions are summarised in Section 5. For file storage purposes, FITS imaging has been compressed/uncompressed using both the NASA HEASARC FPACK/FUNPACK compression format (Pence et al. 2009, 2010) and the GNU Gzip³ compression format⁴. All data and associated code produced for use within this study has been archived on the ZENODO open-access repository⁵.

2 SIMULATED DATA

To test various sky estimation routines, we require an input dataset with known quantities such as sky level and source profile type. We therefore construct a series of simulated images using the GALSIM (Rowe et al. 2015) software. All images consist of a flat sky level with a flux pedestal of zero counts. A series of simulated sources are injected

into these data spanning three different binary configuration modes: source population, source density, and source profile type. For source population, the simulated field is generated in two modes: once containing all sources from the bright end down to the faintest limit explored in this study ($m_{r,\text{total}} = 30$ mag), and a second time excluding the typically undetected faint sources which largely constitute the extragalactic background light. For source density, both low- and high-density fields are simulated. Finally, for source profile type, both disk-like exponential and more extended de Vaucouleurs type sources are injected. For the sake of simplicity, we opt to populate these regions with extended-type Sérsic (1963, 1968) sources alone, avoiding the additional complication of point sources which typically contribute less to sky estimation errors (excepting the extreme bright-end population of stars) than extended profiles. Taking all three binary-type configurations into account, our final simulated dataset consists of eight simulated fields. These simulated fields are shown in Figure 1.

Each simulated region is designed to mimic a single Hyper Suprime-Cam (HSC, Miyazaki et al. 2012, 2018) Subaru Strategic Program (SSP, Aihara et al. 2018a) Public Data Release (PDR1⁶, Aihara et al. 2018b) patch, spanning exactly 4200×4100 pixels in dimension (approximately $706'' \times 689''$). Following a series of tests, tract-patch 8283-38 was selected as a basis for the low density region, whilst tract-patch 9592-20 was selected as a basis for the high-density region. The SOURCE EXTRACTOR software package is used to generate initial source catalogues across these two fields. Further information on the selection procedure of these two fields and their analysis may be found in Section A.

Figure 2 shows the number of sources per square degree and per magnitude as a function of apparent r -band magnitude. The low density region is shown in the left panel, and the high density region in the right panel. The detected populations from our basis datasets are shown using bold solid outline histograms. Using these detections, simulated sources which map to the thin solid log-linear lines are constructed.

In both the low- and high-density region, the simulated population may be subdivided into three distinct regimes: bright mock sources ($m_r < 22$ mag); detected & used sources ($m_r > 22$ mag), and; faint missing sources ($m_r > 25$ mag). Further information on these simulated data may be found in Section B. In brief, detected sources fainter than $m_r = 22$ mag are taken as-is, with their measured parameters used to construct simulated sources. A log-linear trend line is fitted to the detected population in the magnitude range $22 < m_r < 25$, with the faint end limit chosen as the magnitude at which the detected population begins to become incomplete and turn over. The bright end extrapolation of this trend line determines the bright mock sources injected into these simulated data. Bright detected sources are not directly used, owing to a greater uncertainty on their measured parameters. Finally, a faint-end extrapolation of the fitted trend line is used to generate faint sources down to $m_r = 30$ mag.

³ <https://www.gnu.org/software/gzip>

⁴ With the former preferred for noisy float-type imaging and the latter for integer-type or truncated floating point data.

⁵ <https://doi.org/10.5281/zenodo.7067465>

⁶ <https://hsc-release.mtk.nao.ac.jp>

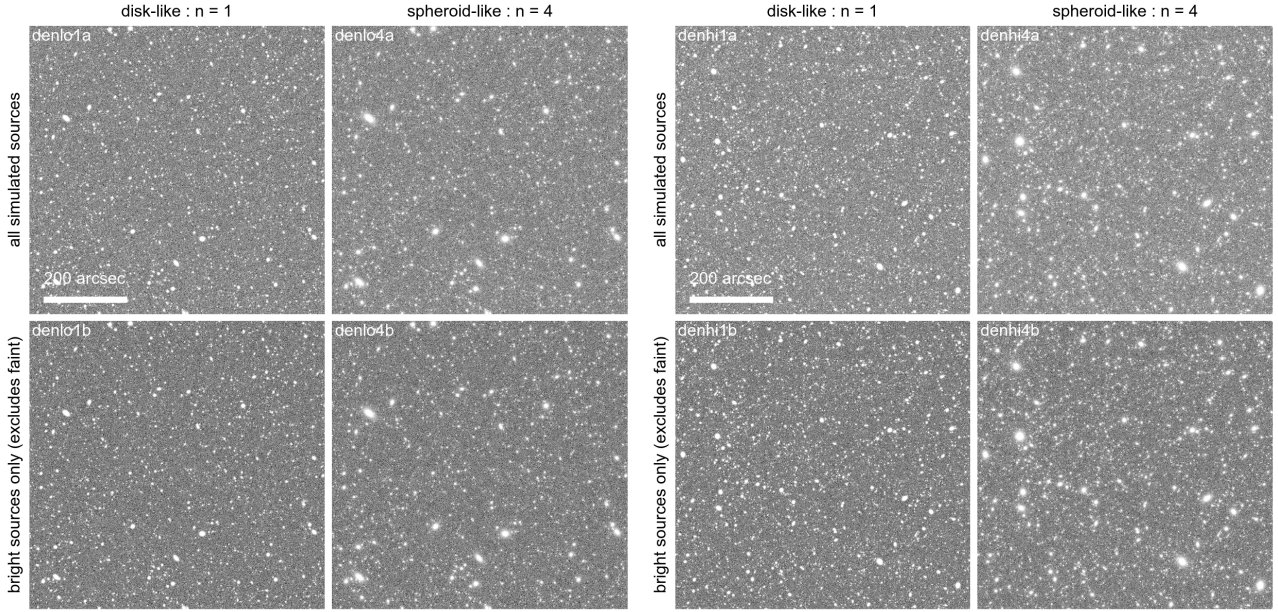


Figure 1. All eight simulated GALSIM fields for the low density ‘denlo’ region (left four panels) and the high density ‘denhi’ region (right four panels). Fields containing only disk-like exponential ($n = 1$) or spheroid-like de Vaucouleurs ($n = 4$) sources are identified by the labels at the top of the figure. Fields containing the full simulated sample or the bright-end sub-population only (i.e., excluding faint missing sources) are labelled along the left side of each density quartet. The scale inset into the top left panel of each density quartet applies equivalently to all panels. All sources are PSF-convolved, and Poisson noise equivalent to HSC-SSP data has been added. Images are arctan scaled. The impact of source population (i.e., contrasting the top row with the bottom) and source profile type (column-to-column) is visibly evident on the apparent background level.

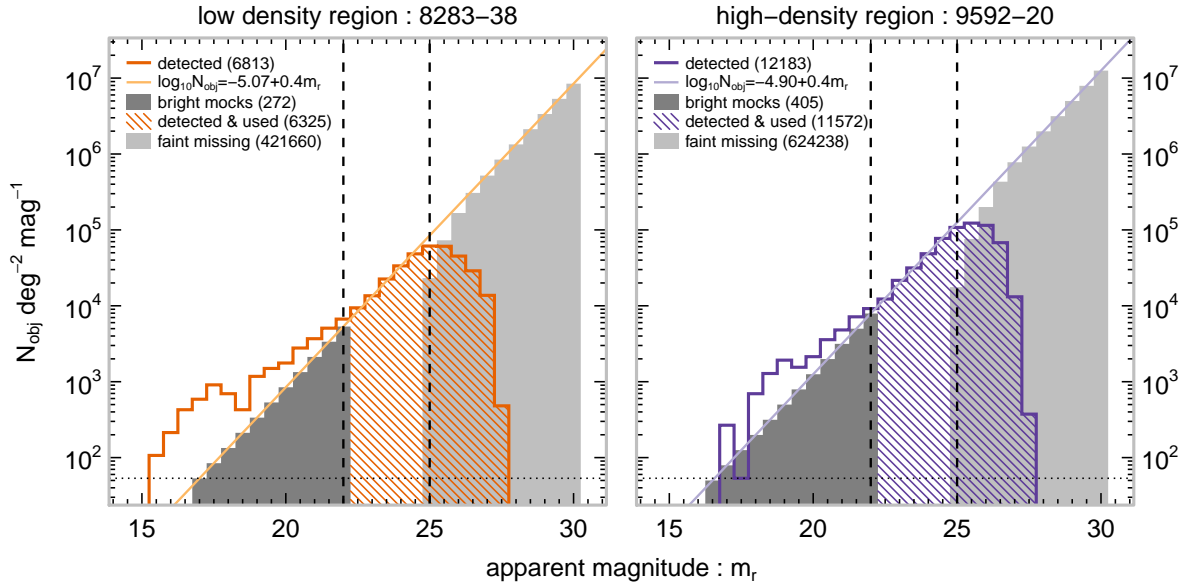


Figure 2. The number of sources per square degree per magnitude as a function of apparent r -band magnitude. The low density region (tract-patch 8283-38) is shown in the left panel, whilst the high density region (tract-patch 9592-20) is shown in the right panel, as indicated. Within each panel, the detected source number density profile is represented as a solid emboldened line. A log-linear best fit line to the detected source profile in the range $22 < m_r < 25$ mag (boundaries represented by vertical dashed lines) is shown using a solid thin line. The dotted horizontal line is equivalent to one object per the area of our sample region per magnitude. Detected sources which are directly used in the simulated input catalogue (detected & used) are found within the hatched area. Simulated sources at the bright end ($m_r < 22$ mag; bright mocks) and faint end ($m_r > 25$ mag; faint missing) are shown using dark grey and light grey shaded regions, respectively. These sources are defined such that their summation in addition to any relevant detected & used sources is equivalent to the fitted log-linear best fit line. Total object numbers for each regime in addition to best fit line parameters are shown in the inset legends. The three flux-associated populations defined here are used to define our input simulated number densities as a function of magnitude.

3 SOURCE EXTRACTION AND SKY ESTIMATION TECHNIQUES

We make use of three distinct source extraction software packages: SOURCE EXTRACTOR, GNU ASTRONOMY UTILITIES (GNUASTRO), and the Rubin Observatory LSST SCIENCE PIPELINES (Bosch et al. 2018, 2019, hereafter, LSST PIPELINES). These three packages are chosen due to their significant usage within the astronomy community at large, and (notably in the case of the LSST PIPELINES) due to their anticipated importance in the reduction of future datasets.

Both SOURCE EXTRACTOR and GNUASTRO are initially operated in a default mode configuration to provide a baseline comparison as to its capabilities. As is common in the literature, each package is further run in various configuration modes with the aim of trying to optimally extract the background sky and generate high-quality source catalogues. As a reminder, simulated background sky maps are flat with a flux pedestal of zero counts. An optimal recovered sky map would therefore return a sky level around zero and relatively uniform in nature.

The LSST PIPELINES are operated in two default configurations to replicate the behaviour of the LSST PIPELINES at or around the time of the publication of HSC SSP PDR1 data (our basis dataset). As a caveat, we note that a number of significant improvements in the sky estimation capabilities of the LSST PIPELINES have taken place since HSC SSP PDR1 data was released, however, we stress that the precise form of the data used to build our simulated dataset is largely irrelevant here. As real HSC data is only being used to initialise a simulated dataset constructed by GALSIM, we would not expect any of our primary conclusions to change should we adopt more recent data released as part of the HSC SSP. We therefore provide these benchmark results by way of comparison, and to facilitate the discussion surrounding sky estimation and source characterisation.

The following sections present two novel techniques aimed at assisting in sky estimation: dilated masking and modelled masking. Subsequent sections provide specific details on each distinct configuration mode explored within this study.

3.1 Magnitude Dependent Dilated Masking

As shown in Ji et al. (2018), insufficient masking of bright extended sources can overestimate any estimation of the background sky. Flux in the wings of such sources can easily leak out beyond a segmentation mask, causing a sky estimation algorithm to interpret these pixels as sky and erroneously attempt to subtract the associated flux. This effect is catastrophic for those interested in low surface brightness science, as it removes much of this LSB signal before scientific analyses can occur. Here we present the dilated masking method, a means by which such flux can be accurately accounted for in order to mitigate the effect of sky over-subtraction.

Dilated masking refers to the process of enlarging the segmented mask map associated with a particular object in such a way that those pixels containing flux from the wings of the source are brought underneath the mask. It is often beneficial to vary the amount of such dilated masking according to the magnitude of the underlying source, as in Ji et al. (2018), with brighter source masks dilated by a

greater amount. Following experimentation with our input simulated dataset and software packages, we opt to expand the segmentation mask about a given detected object by a number of pixels⁷ d , where the extent of d is related to its detected r -band magnitude m_r as given by the following equation:

$$d = \lfloor 10^{-0.2(m_r - 25)} \rfloor + 5 \quad (1)$$

Relative to a bright source, progressively fainter objects have their segmentation mask expanded by decreasing amounts, with the power law component of d flattening out to zero pixels at magnitudes fainter than $m_r = 25$ mag. Each masked region is additionally expanded by a fixed pixel amount of 5 pixels. Segmentation masks are expanded using the GNUASTRO ARITHMETIC software package. Masks are dilated one pixel at a time, alternating between 8-connected dilation and 4-connected dilation, in order to ultimately achieve a dilated mask which isn't biased toward either procedure. The implementation of this dilated masking prescription as applied to SOURCE EXTRACTOR and GNUASTRO outputs is shown in Section 3.3.3 and Section 3.4.3, respectively.

3.2 Modelled Masking

Modelled masking describes the process of constructing a parametric model for select sources, subtracting them from the science image, and reattempting background estimation on the residual image. The generation of a parametric model allows for the extrapolation of such a profile out to large radii and into the noise, rather than using a pixel mask which truncates at a hard isophotal value. Such a concept is not new, with a similar approach previously used in the SDSS (Lupton et al. 2001; Aihara et al. 2011; Blanton et al. 2011). There, two-dimensional ‘cmodel’ galaxy source models are subtracted from the image in order to improve their estimate of the sky, with the outer parts of galaxies considerably more extended than had been before. It's especially important for the chosen form of the model to sufficiently mimic the observed data in the wings of the source, as choosing an inappropriate model may degrade any estimate of the sky rather than improve it.

We opt to model all detected sources brighter than $m_r = 25$ mag with a PSF-convolved single Sérsic profile. The Sérsic (1963, 1968) profile has long been successfully used to describe galaxy surface brightness profiles for a wide range of galaxy types (e.g., Caon et al. 1993; Trujillo et al. 2004; Graham & Driver 2005; Hill et al. 2011; Simard et al. 2011; Kelvin et al. 2012, 2014a,b). Furthermore, our input simulated data have been generated using a range of PSF-convolved Sérsic profiles as described in Section B. As a caveat, whilst fitting Sérsic models to sources with a known Sérsic profile is a best-case scenario (with true galaxies likely more complicated than this), adopting PSF-convolved Sérsic models as our base descriptor of source surface brightness profiles allows us to make a direct comparison of sky estimation software packages without needing to account for potential model inaccuracies. Our rationale for limiting model fitting to bright sources alone is twofold. Firstly, if extended sources do act to negatively impact sky estimation routines,

⁷ The pixel scale of HSC data is 0.168 arcsec/pixel

then it's the brightest of these sources with their broad wings overlapping other sources that will have the largest per-object impact overall. Secondly, bright sources contain a larger number of pixels above the noise threshold. As a consequence, their resultant best-fit models are therefore of a higher certainty.

All detected sources brighter than $m_r = 25$ mag are fit using the SOURCE EXTRACTOR software package. Whilst SOURCE EXTRACTOR is well known for its source extraction capacity, its model fitting capabilities are less familiar. In concert with PSFEX, SOURCE EXTRACTOR is able to accurately and rapidly fit multiple model types to either all detected sources or a subset of detected sources⁸. Available model types include a PSF-like point source (POINTSOURCE), an exponential disk-like profile (DISK) and a generic Sérsic-like spheroid profile (SPHEROID). Specifying any of the associated profile fitting parameter names in the input parameter configuration catalogue will enable source fitting. A catalogue generated from an initial default run of SOURCE EXTRACTOR and our previously described PSFEX PSF model (see Section A2) are used as an input. We opt to fit our magnitude-limited subset sources using the SPHEROID SOURCE EXTRACTOR model type⁹.

Once a catalogue of best fit Sérsic parameters is known, we use the GALSIM software package to construct model imaging. Whilst SOURCE EXTRACTOR is also capable of outputting model imaging (using the MODELS check image type), these images were found to contain several edge artefacts that are not easily removed¹⁰. For each source, the SOURCE EXTRACTOR best fit output provides a starting x/y coordinate location, total luminosity, half light radius, axis ratio, ellipticity and Sérsic index. In addition, GALSIM requires the user to specify the postage stamp box size within which the source is generated. As discussed in Section B7, this postage stamp size should ideally encompass the entirety of our simulated image, mitigating potential edge effects. Due to computational expense however, some lower limit must be specified. We once again define a postage stamp size for each source such that the source profile reaches a surface brightness limit of $\mu_r = 35$ mag arcsec⁻² at the extreme outer edge of the box, with a minimum box size of 11×11 pixels. This ensures that any profile boundary falls well within the noise, effectively eliminating its impact on our subsequent analyses. The resultant model image is finally subtracted from the initial science image, providing a new dataset upon which to estimate the sky with most of the bright source contaminant flux removed. The implementation of this modelled masking procedure as applied to SOURCE EXTRACTOR and GNUASTRO outputs is shown in Section 3.3.4 and Section 3.4.4, respectively.

⁸ Subsets of the total detection catalogue are defined via source matching to x/y coordinates and magnitude as provided by an ASSOC catalogue.

⁹ Complete SOURCE EXTRACTOR catalogue parameters used for fitting in this instance are: NUMBER, X_IMAGE, Y_IMAGE, FLUX_SPHEROID, MAG_SPHEROID, SPHEROID_REFF_IMAGE, SPHEROID_ASPECT_IMAGE, SPHEROID_THETA_IMAGE, SPHEROID_SERSICN, CHI2_MODEL, FLAGS_MODEL and VECTOR_ASSOC. Further information may be found in Bertin & Arnouts (1996) and associated documentation.

¹⁰ We direct the interested reader to Section F for further details.

3.3 Source Extractor Configurations

3.3.1 Default SOURCE EXTRACTOR Configuration

The default setup of SOURCE EXTRACTOR used at this stage of processing is identical to that outlined in Section A1, with the convolution kernel, stellar classification neural network file and configuration file all the same. The threshold for source detection is maintained at 1.5σ of the background estimate. Having excluded detected sources, background sky in SOURCE EXTRACTOR is estimated across the image within a default of 64×64 pixel BACK_SIZE mesh elements. A bicubic-spline interpolation is subsequently applied to all mesh elements to produce a background map, allowing for the exclusion of erroneous mesh values. In addition to the output catalogue parameters defined in Section A1, we also opt to output ISOAREA_IMAGE, providing data on the total area above the analysis threshold for each detected object. The SOURCE EXTRACTOR package is run upon each simulated image, producing an output catalogue and check images for the segmentation map (SEGMENTATION), background pedestal map (BACKGROUND) and background RMS map (BACKGROUND_RMS). Further information on the default operation of SOURCE EXTRACTOR may be found in Bertin & Arnouts (1996).

3.3.2 Modified SOURCE EXTRACTOR Configuration

The SOURCE EXTRACTOR package is often modified in order to better tailor its outputs to the specific scientific needs of the input dataset. A sky estimation and source detection setup which may prove optimal for the characterisation of point-like sources is often wholly inadequate for the purposes of extended source analysis. Modifications are also often made to address common complaints with the default outputs of SOURCE EXTRACTOR (see, e.g., Häußler et al. 2007; Häußler et al. 2013; Simard et al. 2011; Barden et al. 2012; Kelvin et al. 2012; Hiemer et al. 2014). Principal amongst these are issues surrounding the derived sky level, an inadequate smoothing kernel, and inaccurate source segmentation. There is a long and inglorious history to such segmentation failures in top-down auto-detect algorithms. For a number of years in the field of Source Extraction (see e.g. FOCAS, Jarvis & Tyson 1981) such segmentation failures have often been encountered when using low threshold runs of SOURCE EXTRACTOR, largely in situations where there is a triangle of objects that fail proper segmentation and photometry. This geometry can create a situation where there is no 1-D saddle point in the surface brightness.

We adopt five key SOURCE EXTRACTOR configuration modifications to address these issues. First, we increase the background mesh element size (BACK_SIZE) to 128×128 pixels (from a default of 64×64 pixels). An increase of this type reduces the risk that any individual mesh element becomes severely compromised by source flux from a single bright object or cluster of bright objects. Second, we also increase the background mesh filter size (BACK_FILTERSIZE) to 5 (from a default of 3). This filtering size determines the mesh super-pixel area over which mesh elements are filtered to detect and eliminate background estimate outliers. A larger filter size increases the identification of outliers, providing a more coherent global sky estimate. Third, to assist with initial source detection, we reduce the detection and analysis thresholds (DETECT_THRESH and ANALYSIS_THRESH) to 0.5σ

(from a default of 1.5σ), and fourth, we replace the default smoothing kernel with a Gaussian of FWHM $\Gamma = 2$ pixels. A larger smoothing kernel reduces the impact of contaminant noise spikes present within the background and allows for a lower overall source detection threshold. Finally, we reduce the minimum segmentation contrast parameter (DEBLEND_MINCONT) to 0.00005 (from a default of 0.005). Reducing this value increases the chance that faint local peaks will be included as separate objects. Whilst this does not directly impact the final sky estimate, it does produce superior segmentation results within contiguous regions falling above the detection threshold, necessarily improving source extraction catalogue data.

3.3.3 SOURCE EXTRACTOR with Dilated Masks

It is not natively possible to apply the dilated masking process outlined in Section 3.1 within SOURCE EXTRACTOR itself. Implementation of this procedure therefore requires modifying the data that is fed into SOURCE EXTRACTOR. First, dilated masks are produced using outputs from a default SOURCE EXTRACTOR run. Using the input science image, each dilated masked pixel is set equal to NaN. Such pixels will not be used by SOURCE EXTRACTOR to construct a background map. This new manually masked image is processed using the same default SOURCE EXTRACTOR setup as previously used.

An example of the dilated masking routine as applied to simulated data processed by SOURCE EXTRACTOR is shown in Figure 3. The top-row left panel shows a zoomed in $n = 4$ low density simulated field (denlo4a), arctan scaled and smoothed with a Gaussian kernel of $\Gamma = 3$ pix. The middle-row left panel shows the segmentation map for this region as produced using a default SOURCE EXTRACTOR run. Each segmented region is colour coded according to the total detected r -band magnitude of the underlying source, as represented by the inset colour bar. The top-row central panel shows the default SOURCE EXTRACTOR segmentation map overlaid upon the initial image, whilst the middle-row central panel shows our magnitude dependent dilated masks overlaid upon the initial image. Finally, the top-row and middle-row right panels show the output background sky maps as determined using the original default segmentation map and the new dilated mask map, respectively. Bottom-row panels are discussed in the next section.

As shown, a significant amount of flux is evidently leaking from the outskirts of the default segmentation map. Further, the amount of flux leakage appears linked to the brightness of the underlying source, with the majority of the contamination in this particular field linked to the large bright source in the upper right corner. As these initial simulated fields consist of a flat and equal to zero background map, recovery of a faint and relatively uniform background model is preferred. In this case, application of magnitude-dependent dilated masks significantly reduces the amount of contaminant flux present in the remaining background pixels, markedly improving the resultant background sky estimate.

3.3.4 SOURCE EXTRACTOR with Modelled Masks

Following an initial run of SOURCE EXTRACTOR and GALSIM in order to generate free-Sérsic models for all sources brighter than $m_r = 25$ mag, the model plane is subtracted from the science image to produce a residual image. The removal of bright source wings allows for a more accurate estimate of the sky in these regions, whilst simultaneously markedly improving source characterisation for small faint sources previously hidden beneath the wings of their bright neighbours. The centres of bright astrophysical sources are notoriously difficult to fit, with even a slight model inaccuracy resulting in a pixel value offset of many multiples of the background RMS. To prevent such regions having any impact upon our sky estimation routine, we manually apply the original default SOURCE EXTRACTOR segmentation mask to the residual image, setting masked pixels equal to NaN. Consequently, centroid pixels are ignored by SOURCE EXTRACTOR when generating sky estimates and whilst performing source extraction.

An example of the modelled masking routine as applied to our simulated data is shown in Figure 3. The top and middle rows have already been discussed in the prior section, showing the original simulated image, the original background map, and the dilated masking results. The bottom row left panel shows the fitted PSF-convolved Sérsic model plane generated for this region. All detected sources brighter than $m_r = 25$ mag are fitted. The bottom row centre panel shows the residual image generated once the fitted model is removed from the original image, also with the original mask map overlaid. As can be seen, much of the contaminant flux leaking out from the segmented regions has been successfully accounted for. The bottom right panel shows the background sky resulting from a model masked processed image. The difference between this background map and the original is obvious, with multiple orders of magnitude difference in the resultant background sky estimate. As these simulated data consist of a flat and equal to zero sky pedestal, the background map produced via the modelled masking procedure is clearly outperforming the other methods shown here. Notably, the impact of the singular bright source has been almost completely accounted for, leaving behind a much more uniform sky estimate in its place.

3.4 Gnuastro Configurations

3.4.1 Default GNUASTRO Configuration

The GNUASTRO software suite is highly modularised, necessitating the use of several sub-packages to fully process any given dataset. Each simulated image is initially processed by NOISECHISEL, the GNUASTRO source detection and sky estimation package designed to optimally extract sources with extended profiles embedded within noisy data. In brief, pixel data is first convolved with a Gaussian smoothing kernel and thresholded at some pixel value quantile (e.g., the 30th percentile) within mesh elements of default size 30×30 pixels, splitting the image into regions of noise and regions of signal. A series of erosions and dilations are subsequently performed on the regions of noise (i.e., the noise is ‘chiselled’ away) and false detections are removed. Any remaining regions of signal undergo further pixel dilation. Once regions believed to contain true signal flux are determined, the SEGMENT package

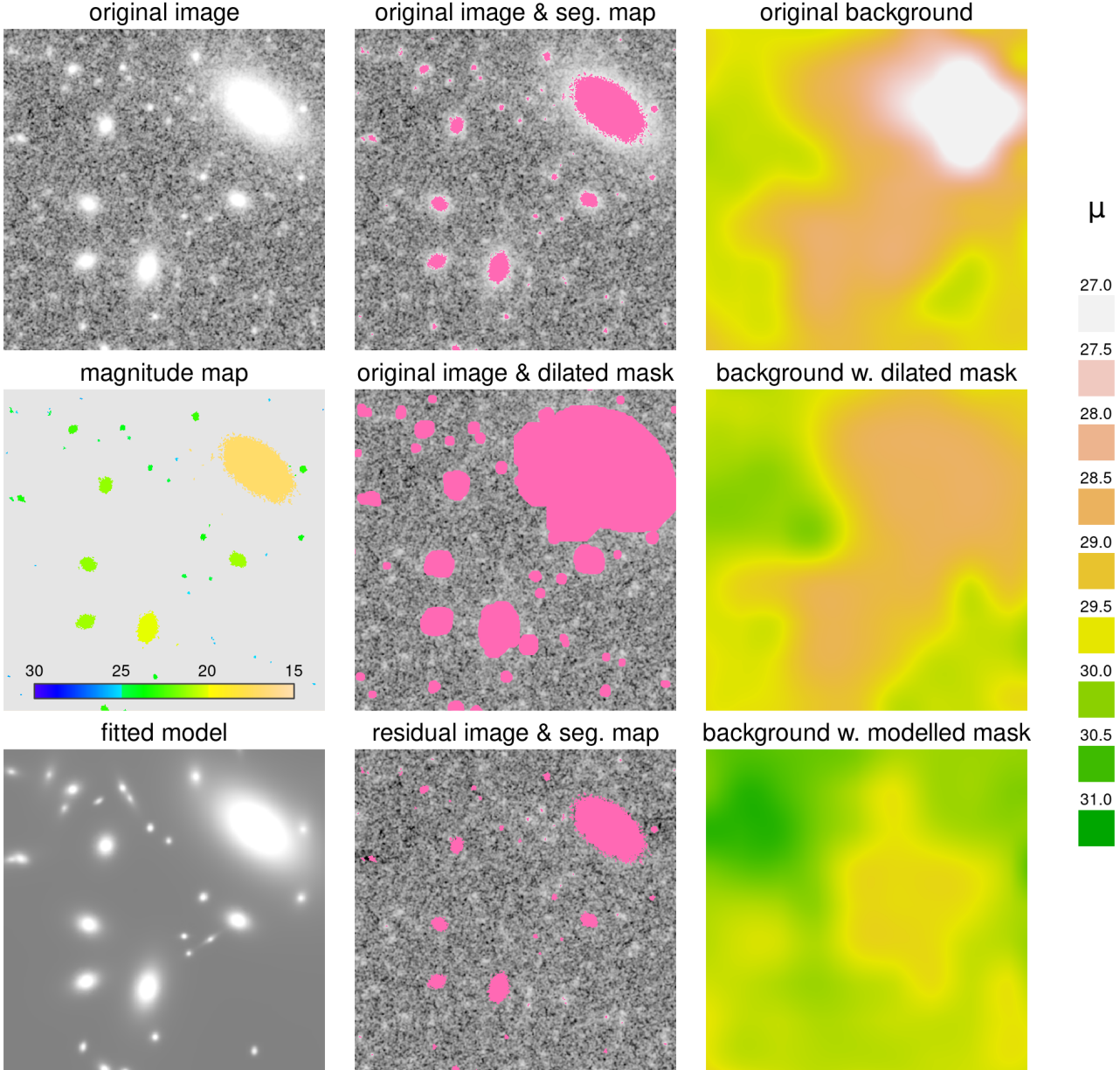


Figure 3. Examples of dilated masking and modelled masking sky estimation techniques as applied to a low density simulated field and processed using the SOURCE EXTRACTOR software package. Top row, left: the original simulated dataset, corresponding to a zoomed in section of the low density field shown in Figure 1. Top row, centre: the original segmentation map overlaid upon the original image. A significant amount of flux can be seen leaking out beyond the default segmented regions, thereby contaminating any estimate of the sky. Top row, right: the original estimate of the background sky as found when using default segmentation masks. A notable contamination due to the bright extended source within this field is evident. Middle row, left: the segmentation map for this region as given by a default run of SOURCE EXTRACTOR. Each segmented region is colour coded according to its underlying detected source magnitude, as shown by the inset colour bar. Middle row, centre: the new dilated mask overlaid upon the original image. The extent of mask dilation is magnitude dependent, as given by Equation 1. These larger dilated masks are superior at masking signal around the wings of bright sources. Middle row, right: the new estimate of the background sky as found when using the dilated masks shown here. Much of the aforementioned background sky contamination is improved, resulting in a flatter and more accurate sky estimate. Bottom row, left: the successfully fitted single Sérsic models based upon detected sources brighter than $m_r = 25$ mag. Bottom row, centre: the residual image generated after the fitted model is removed from the original image, overlaid with the default SOURCE EXTRACTOR segmentation map. Note how much of the prior contaminant flux observed leaking from beyond the edge of the segmented regions has been removed. Bottom row, right: the new estimate of the background sky generated when using modelled masks. Colours correspond to surface brightness levels in units of mag arcsec^{-2} shown in the outlying legend. The sky estimate is significantly improved relative to both the default sky map and the dilated mask sky map, no longer exhibiting strong source-correlated sky biases. Images are arctan scaled, with noisy imaging smoothed by a Gaussian kernel of $\Gamma = 3$ pix.

splits these regions into distinct sources, performing clump-based segmentation where required.

The SEGMENT package assigns pixels into one of three distinct types: noise, clump, and object. Noise regions are those where no significant signal from physical objects have been detected. Clumps are connected regions associated with local maxima on the image. Objects correspond to all pixels which are believed to contain physical object flux. Each object may contain zero, one, or many distinct clumps, and clump information is used to assist in object segmentation (see Akhlaghi & Ichikawa 2015, for further information). As the focus of this study is on the optimal extraction of the background sky, our primary interest is the distinction between signal and noise. We therefore opt here to utilise the object catalogues for further study throughout.

Once segmentation has been finalised, the MAKECATALOG package is used to convert processed pixel data into an output source catalogue¹¹. Further information on the operation of all GNUASTRO packages may be found in Akhlaghi & Ichikawa (2015), with subsequent updates in Akhlaghi (2019).

3.4.2 Modified GNUASTRO Configuration

As with SOURCE EXTRACTOR, a number of modifications are typically made to the operation of GNUASTRO to improve or tailor its output results. Owing to the modularised nature of GNUASTRO, some modifications are made to all utilised sub-packages, whilst others are specific to individual sub-packages. We detail all modifications here.

First, as with SOURCE EXTRACTOR, we opt to increase the default mesh size of 30×30 pixels used during initial background estimation using the `tilesize` argument. The tile size determines the mesh size within which initial background thresholding occurs. In the presence of large sky gradients or large contaminant sources, an overly-large tile size may lead to a significant amount of data either being discarded or erroneously classified by NOISECHISEL. However, a larger mesh size will also reduce the chance that any single mesh element is entirely dominated by signal flux, and enforce the generation of a flatter and inherently less-responsive sky model. During testing, the recovered sky level appeared to be somewhat unresponsive to the choice of mesh size (within a factor of 2 of the default value), having a relatively larger impact only on the RMS of the background map. Therefore, in keeping with the logic previously used with SOURCE EXTRACTOR, we opt to increase the tile size to 64×64 pixels¹². The tile size parameter is globally provided to NOISECHISEL, SEGMENT and MAKECATALOG.

Second, we opt to reduce the threshold down to which

¹¹ Output GNUASTRO MAKECATALOG columns are: `ids`, `x`, `y`, `brightness`, `magnitude`, `semimajor`, `semiminor`, `geosemimajor`, `geosemiminor`, `sn`, `axisratio`, `positionangle`, `sky`, `std`, `area` and `upperlimit`. A full description for each column output may be found in Akhlaghi & Ichikawa (2015) and Akhlaghi (2019)

¹² An attempt was also made to increase the GNUASTRO tile size to 128×128 pixels, in keeping with the modified SOURCE EXTRACTOR runs discussed previously. Unfortunately however, these runs fail with some of our input datasets, with GNUASTRO reporting that not enough neighbours could be found for close neighbour interpolation.

NOISECHISEL detection maps are expanded using the `det-growquant` parameter. The detection growth quantile (default 0.9) determines down to what quantile ‘true’ detections are expanded out into the noise. This growth mechanism has potential advantages over a traditional dilation, as it allows the user to follow the shape of the profile out into the noise. Such an effect is crucial in accurately capturing more of the diffuse low surface brightness light typically located around the wings of bright extended sources. However, setting this value too low leaves open the possibility that spurious noise signals will end up being drawn into the final resultant detection maps, artificially inflating the flux associated with detections. We opt to lower the detection growth quantile parameter to 0.7, somewhat expanding our detection footprints relative to the defaults to capture more of the potential low surface brightness flux.

We note that a number of additional parameters were explored and rejected here, owing to their failure to significantly improve sky estimation or source extraction results during testing. These include modifications in: the smoothing kernel (`KERNEL`), the maximum mean and median quantile difference per tile (`MEANMEDQDIFF`), the quantile threshold on the convolved image (`QTHRESH`), the quantile threshold determining which pixels are excluded from erosion (`NOERODEQUANT`), the selection of sky tiles (`MINSKYFRAC`), and quantile of the signal-to-noise ratio distribution of clumps in undetected regions (`SNQUANT`).

3.4.3 GNUASTRO with Dilated Masks

Figure 4 shows the dilated masking routine as applied to simulated data which has been processed by GNUASTRO. Each panel is equivalent to the panels previously shown in Figure 3, excepting that the segmentation maps and subsequent dilated masks (and model masks, discussed in the next section) are based upon GNUASTRO source extraction processing. As above, the effect of the dilated masking procedure is to notably reduce the impact of flux leakage upon the final background sky estimate. As these simulated data have been constructed with a flat and equal to zero sky, a faint and uniform background model is optimal here. We also note however that the original segmented region produced by GNUASTRO covers a much larger fraction of the original image than was the case with SOURCE EXTRACTOR. Consequently, the original default background sky produced by GNUASTRO is markedly less impacted by the bright source in this region than the default outputs from a SOURCE EXTRACTOR run. This will be further discussed in Section 4.

3.4.4 GNUASTRO with Modelled Masks

Figure 4 (bottom row) shows the effect of modelled masking as applied to simulated data which has been processed by GNUASTRO. Simulated data have been constructed with a flat and equal to zero sky pedestal. As above, each panel is equivalent to the panels previously shown in Figure 3, except that the segmentation maps and derivative modelled mask data are based upon GNUASTRO source extraction processing. The impact of modelled masks appears to have a negligible impact on the resultant background map. With the initial segmentation map already reasonably extensive, as

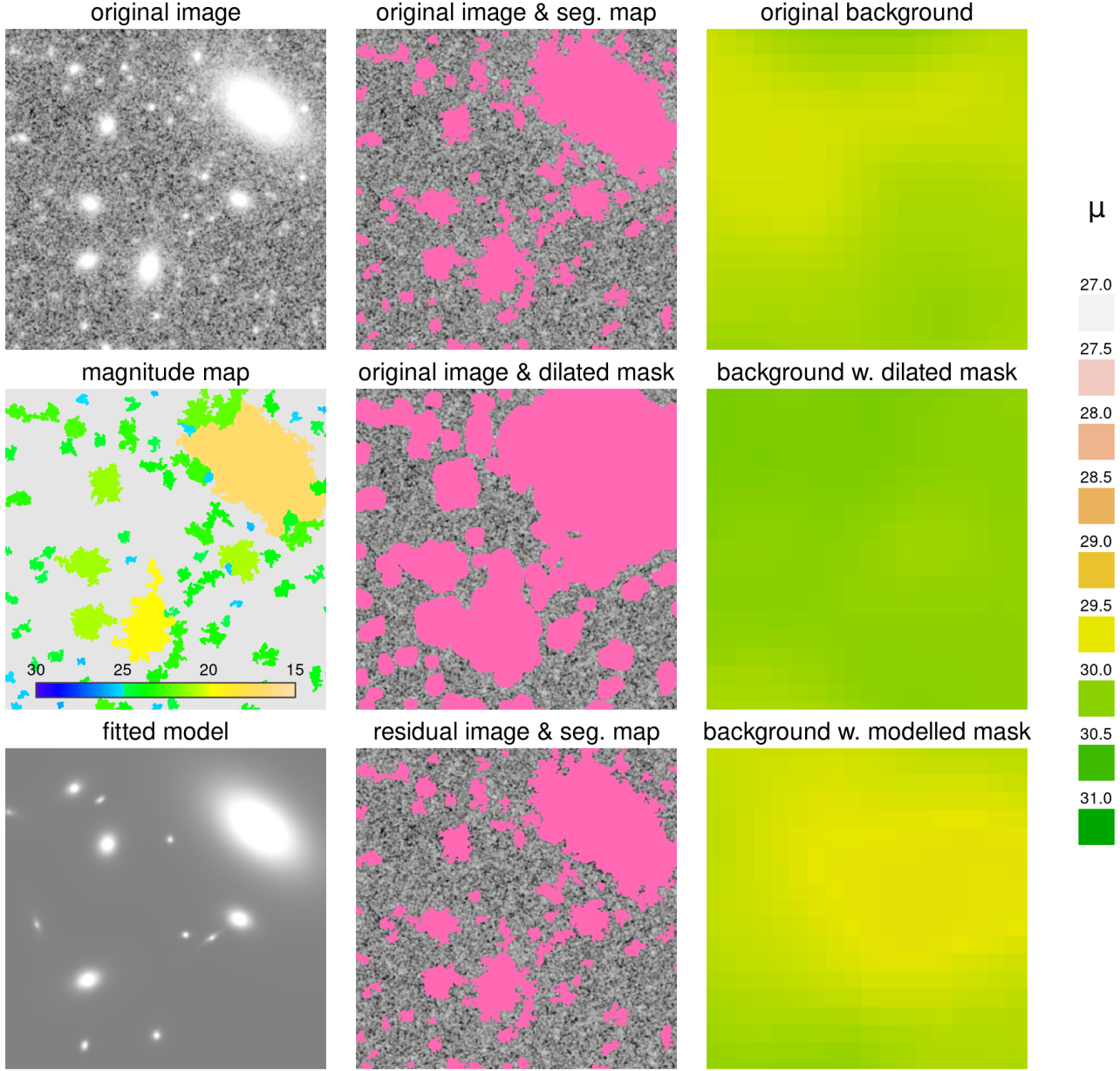


Figure 4. As Figure 3, but for simulated data initially processed using the GNUASTRO software package.

noted above, the model masking procedure has little extra to contribute. A more complete discussion of the impact of modelled masking will be further discussed in Section 4.

3.5 Configurations of the LSST Pipelines

The Rubin Observatory LSST PIPELINES were designed to optimally process HSC and LSST type imaging, providing a suite of complex image processing routines to ultimately produce high fidelity output catalogue and imaging data. This software stack has been working with HSC data since HSC’s first light, making it an ideal candidate for use with the simulated HSC-type imaging produced for this study. We process our simulated data with two version 19.0.0 configurations of

the LSST PIPELINES. First, these data are analysed with a specific configuration of the LSST PIPELINES designed to mimic an earlier state of the code base utilising a sixth-order polynomial fit to describe the background model. The code base at this time is largely equivalent to that used to initially produce HSC-SSP PDR1 data, and serves as a useful baseline. Second, we process our simulated datasets with an updated configuration of the LSST PIPELINES which employs a more local 128-pixel spline to describe the background model. Both configurations are further discussed in the sections below, with full details to be found in Bosch et al. (2018) and Bosch et al. (2019).

3.5.1 LSST PIPELINES Sixth Degree Polynomial Configuration (P6)

The first configuration of the LSST PIPELINES explored here is one which generates a background map using a sixth degree polynomial fit to detected background pixels (hereafter referred to as ‘P6’, for brevity). Simulated image data is initially convolved with a smoothing kernel, and contiguous regions above some threshold level are identified. In a standard run of the LSST PIPELINES (i.e., using true astrophysical data), high signal-to-noise stars are identified on the stellar locus using a placeholder Gaussian PSF to perform a first detection pass. These bright stars are then used to model the spatially varying PSF over the image using PSFEX. A circular Gaussian whose RMS width is matched to the PSF is used as a detection kernel for performance reasons. However, as the simulated imaging constructed for use within this study contains no point sources (see Section B) we do not follow this procedure here. Instead, we construct a circular Gaussian whose RMS width is matched to the PSF described in section A2. This circularised Gaussian is subsequently used as the primary detection kernel.

Background estimation within the LSST PIPELINES is handled by the SUBTRACTBACKGROUNDTASK method. The astrophysical background contains contributions from several sources: the night sky, optical ghosts and scattered light in the telescope, and undetected sources that make up the EBL amongst them. A parametric model based upon the sum total of these contributions to the background is constructed and subsequently subtracted out at the image level. The process consists of two high-level steps. First, the image is subdivided into 128×128 pixel bins, or *super pixels*. Pixels which constitute each super pixel and do not correspond to any detected object are used to calculate the mean, variance, and pixel averaged centre of its host super pixel. Second, a 6th order two-dimensional Chebyshev polynomial model is fit to the mean values of the image, using the average pixel centres of each super pixel. Each bin is inverse weighted by its variance such that noisy super pixels with relatively few unmasked regions do not overly bias the fit.

Figure 5 shows the results of the LSST PIPELINES P6 configuration as applied to these simulated data. The top row shows the original simulated image, the returned segmentation map, and the recovered sky map for a zoomed in section. As shown, the sky map is relatively homogeneous, albeit with a brighter sky pedestal than that recorded by some other techniques.

3.5.2 LSST PIPELINES 128-Pixel Spline Configuration (S128)

The second configuration of the LSST PIPELINES explored here generates a background map using a 128 pixel spline fit to all identified background pixels (hereafter referred to as ‘S128’, for brevity). This configuration makes use of an alternate detection algorithm which is better suited towards detecting EBL galaxies and LSB flux. In the LSST PIPELINES P6 configurations, the detection threshold is fixed at 5σ across the whole field, where σ^2 is the variance. However, the variance estimation may be incorrect after convolution owing to the fact that convolution correlates the noise. This leads to an under-performance in the detection algorithm,

where recognisable-by-eye sources are not detected (see Aihara et al. 2019, Figure 5). To mitigate these effects, we run the high level process DETECTCOADDSOURCESTASK in the S128 configuration, which adopts the DYNAMICDETECTIONTASK in the LSST PIPELINES in lieu of the default detection package used in the P6 configuration. In the DYNAMICDETECTIONTASK, mock PSFs are injected into the image in regions of mostly empty sky, ensuring that detected objects are avoided. The ratio between the standard deviation of PSF fluxes of the points to the variance over the effective area of the PSF provides a correction factor to the detection threshold, dynamically adjusting it across the image.

To implement this optimised setup, image data is initially processed in a manner consistent with that described above. Sources are detected, masked, and the remaining simulated imaging is subdivided into 128×128 super pixel bins. A 3σ clipped mean is computed among all non-masked pixels inside each super-pixel, and a two-dimensional 6th order bilinear spline is fit to these super pixel means. This creates a full resolution image of the sky background model. This procedure is designed to be consistent with the operations performed to produce HSC-SSP PDR1 data.

The bottom row of Figure 5 shows the returned segmentation map and recovered background sky for a zoomed in segment of low density simulated data. Whilst fainter sources appear to exhibit segmentation footprints similar in scale to those from the prior P6 configuration, the segmentation footprint for the brightest source in this region is notably smaller in area. This has a significant impact on the recovered background map, as shown. However, excepting such bright source contamination, the overall recovered sky is significantly fainter here than with the P6 configuration.

4 RESULTS

The procedures above provide background sky estimates and source detection results for a number of simulated datasets. A total of eight HSC-SSP PDR1 fields consisting of a flat and equal to zero sky level are simulated in three binary flavours: fields with faint EBL sources either included or excluded; fields of either a high or a low source density; and fields populated exclusively with either exponential ($n = 1$) or de Vaucouleurs ($n = 4$) radial profile source types. These data are processed in 10 software configuration modes: four configurations of the SOURCE EXTRACTOR software package, four configurations of the GNUASTRO software suite, and two configurations of the LSST PIPELINES.

Our full sky estimation results are shown in Table 1. Each cell in this table shows the estimated mean and standard deviation (in units of nJy per square arcsec¹³) of the recovered background sky model for each flavour of simulated data (per column) and software configuration mode (per row). As a reminder, all simulated datasets are background subtracted (i.e., the input sky was set to zero), so

¹³ measured counts on an image are converted to the calibrated unit nanoJanskys using the conversion factor 1 count ~ 57.5 nJy. The pixel scale is 0.168 arcsec/pixel. Results are presented in nanoJanskys to facilitate comparison with other datasets and to allow for negative flux values to be presented in the case of background subtracted data.

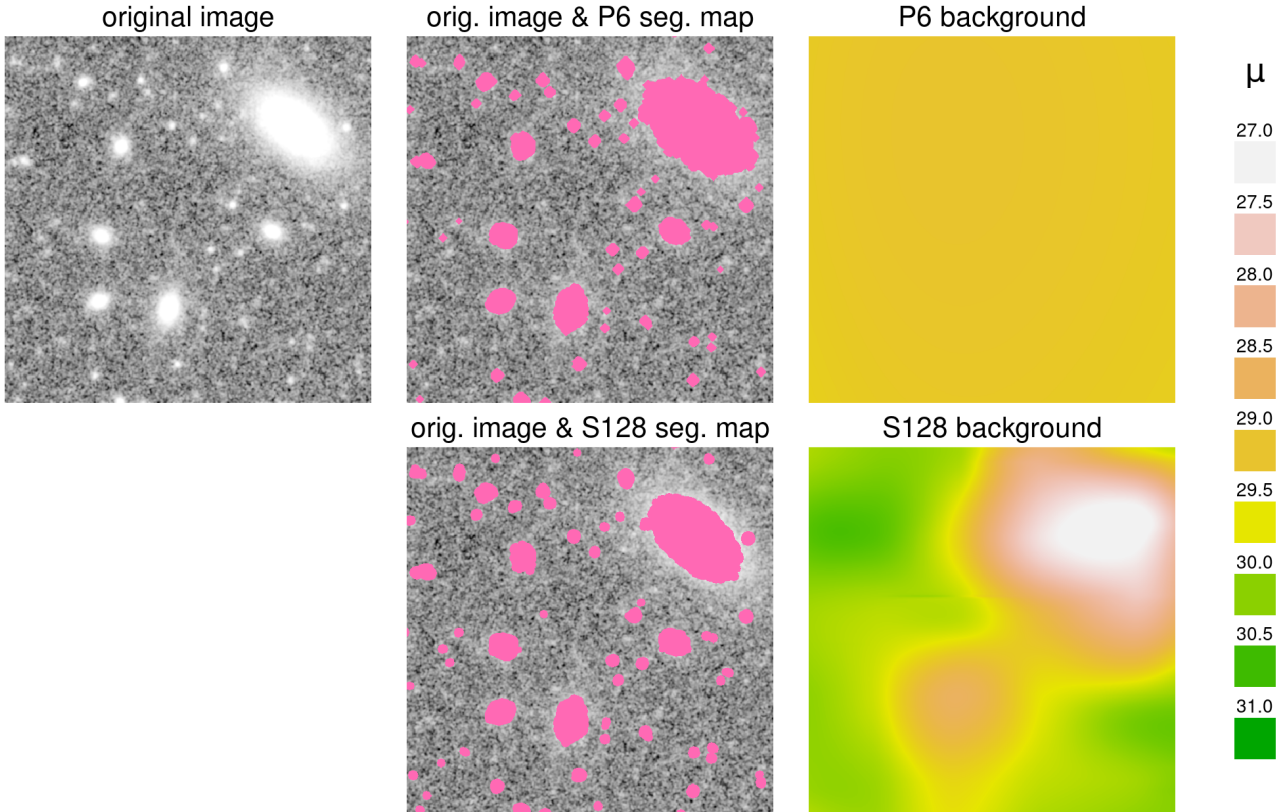


Figure 5. Similar to Figures 3 and 4, but for simulated data initially processed using the LSST SCIENCE PIPELINES. A zoomed-in section of the original simulated image is shown on the left. The central column shows the original simulated image again in the background, with the segmentation maps returned by the P6 (top) and S128 (bottom) methods overlaid. The right column shows the resultant recovered background maps for this small zoomed in section of the sky, again for both the P6 (top) and S128 (bottom) methodologies. Whilst the P6 configuration returns a flatter and more homogeneous sky pedestal, the S128 configuration returns fainter sky levels (albeit with more fluctuation in the recovered sky map).

recovered sky values closer to zero are more desirable here. Common trends become apparent, and are explored below. We begin by discussing global sky estimation trends visible between all flavours of binary data type regardless of any specific software configuration mode in Section 4.0.1. Following this, we then compare each software configuration mode against one another in the context of output sky levels in Section 4.0.2 to discover desirable sky estimation and source extraction techniques. Finally, we move beyond analysis of the output sky levels and sky maps to take a closer look at the fidelity of output source catalogues in Section 4.0.3.

4.0.1 Trends by Flavour: Source Population, Density and Type

Simulated fields with faint EBL sources included always return brighter estimated sky levels than fields with such sources excluded, as might be expected. This is true for all software configuration modes and for all flavours of source population, density and profile type explored here. Many of these faint sources are exceedingly difficult to disentangle from background noise, leading to their being missed from initial source detection and consequently having their flux

entered into background estimation routines. Mischaracterisation of such sources is the single largest contributor to sky estimation offsets, as evidenced here. The effect of including faint background sources causes recovered mean background sky levels to be anywhere from 6.8 to 15.8 nJy arcsec⁻² brighter. This equates to recovered mean background sky levels being brighter when faint EBL sources are included by anywhere in the range $1.8 \leq \sigma \leq 39.5$. On average, recovered sky levels are 9.4σ brighter when faint EBL sources are included. Such large offsets evidence the importance in accounting for extremely faint sources in the first instance, and also underlines the significant role they play in modifying output background models. This effect was also found in Ji et al. (2018), where the sky misestimation produced by a default SOURCE EXTRACTOR run was reduced by 8σ in the case of a random galaxy distribution when using an improved sky background estimator.

The impact of field density on the resultant background model is also significant, with 36 out of the total 40 combinations of software configuration modes and flavours explored here returning a brighter mean background sky in the high density regime than in its equivalent low density counterpart. Notably, all simulated fields with faint EBL sources included return a brighter sky in the high density regime. The

source population : source density : source type : label :	including all sources				excluding faint sources			
	low density		high density		low density		high density	
	1	4	1	4	1	4	1	4
	(denlo1a)	(denlo4a)	(denhi1a)	(denhi4a)	(denlo1b)	(denlo4b)	(denhi1b)	(denhi4b)
SOURCE EXTRACTOR								
default	13.9 ± 3.1	16.7 ± 5.7	20.7 ± 3.3	25.4 ± 6.8	3.6 ± 2.8	5.7 ± 5.6	6.0 ± 3.1	9.9 ± 6.9
modified	14.0 ± 1.7	16.5 ± 2.2	20.9 ± 1.4	24.9 ± 2.5	3.6 ± 1.1	5.6 ± 1.8	6.1 ± 1.4	9.6 ± 2.7
w. dilated masks	10.5 ± 2.1	13.8 ± 3.2	16.0 ± 2.3	20.8 ± 3.3	0.9 ± 1.8	3.2 ± 2.8	1.7 ± 1.8	5.4 ± 3.3
w. modelled masks	8.4 ± 2.6	8.7 ± 3.5	12.4 ± 3.3	12.5 ± 4.5	-1.0 ± 2.3	-1.8 ± 3.3	-1.2 ± 2.6	-2.5 ± 4.3
GNAUSTRO								
default	9.3 ± 1.3	11.6 ± 1.5	13.1 ± 1.6	16.5 ± 1.7	0.4 ± 0.9	1.9 ± 1.1	0.5 ± 0.9	2.6 ± 1.3
modified	7.8 ± 0.8	9.8 ± 0.8	11.1 ± 1.1	14.5 ± 0.8	-0.5 ± 0.7	0.4 ± 0.7	-0.7 ± 0.8	0.7 ± 0.6
w. dilated masks	8.9 ± 1.5	10.7 ± 1.5	12.6 ± 0.8	15.7 ± 1.6	0.1 ± 1.2	1.1 ± 1.2	0.7 ± 1.1	1.2 ± 1.3
w. modelled masks	9.2 ± 1.4	11.2 ± 1.5	13.2 ± 1.6	15.9 ± 1.7	0.2 ± 0.9	1.1 ± 1.3	0.6 ± 1.1	1.9 ± 1.3
LSST PIPELINES								
P6	12.6 ± 0.4	16.1 ± 1.4	18.3 ± 0.5	23.9 ± 1.5	2.2 ± 0.3	5.1 ± 1.3	3.4 ± 0.4	8.1 ± 1.4
S128	10.0 ± 1.5	11.9 ± 4.9	14.2 ± 1.8	19.8 ± 5.9	3.2 ± 1.3	3.3 ± 4.9	0.2 ± 1.5	5.3 ± 6.1

Table 1. Estimated background statistics as determined by various image characterisation software packages. Each column represents a unique flavour of simulated field as defined in Table B1. Each row represents a different sky estimation software package configuration mode as detailed in Section 3. Values shown here represent the output mean and standard deviation in units of nJy arcsec⁻². More accurate (i.e., closer to zero) sky estimation results are consistently recovered in: fields with faint sources accounted for and excluded; fields of relatively low source density, and; in fields comprised of relatively more compact $n = 1$ type sources.

effect of switching from a low density field to a high density field returns mean background sky values anywhere in the range 2.9 nJy arcsec⁻² fainter to 8.6 nJy arcsec⁻² brighter. This equates to recovered mean background sky levels in high density regimes falling in the range 2.3 σ fainter to 15.2 σ brighter, with an average of 2.2 σ brighter. When considering only the more realistic ‘a’-type simulated datasets (i.e., only considering those that also include faint EBL sources), recovered mean background sky levels are brighter in the high density field relative to their low density equivalents anywhere in the range 1.1 $\leq \sigma \leq 15.2$, with an average value of 3.6 σ brighter. These data show that high density fields act to notably impact the sky estimation routines explored here. A higher source density results in a greater number of undetected galaxies that ultimately contribute to contamination of the sky estimate. There are of the order 200000 more galaxies in the high density regime as compared to the equivalent low density regime. As a consequence, not only are more galaxies prone to being lost in the EBL, but a higher number of the brightest of galaxies will also throw extra flux into the background in their bright extended wings.

Finally, source profile type also has a notable impact on resultant background map levels. Of the 40 software configuration modes and flavours compared here, 38 return a brighter sky in those fields populated with $n = 4$ de Vaucouleurs type profiles than in their equivalent $n = 1$ exponential counterparts. As with source density, the subset of fields that include faint EBL sources always return a brighter background sky in the $n = 4$ scenario relative to the $n = 1$ case. Switching from $n = 1$ to $n = 4$ profiles results in estimated background sky levels returned in the range 1.2 nJy arcsec⁻² fainter to 5.6 nJy arcsec⁻² brighter. This equates to $n = 4$ simulated fields being anywhere from 0.5 σ fainter to 12.4 σ brighter than their $n = 1$ equivalents, with an average significance of 2.5 σ brighter. When considering only the more realistic ‘a’-type simulated datasets with faint EBL sources included, recovered background sky maps are brighter in the $n = 4$ case by anywhere in the

range 0.0 $\leq \sigma \leq 11.8$, with an average significance of 2.7 σ brighter. These data show that fields populated with more extended sources often act to increase the resultant estimated background pedestal. Extended de Vaucouleurs type sources contain significantly more flux in their wings than their equivalent exponential-type profiles, with the latter concentrating more of their flux in the relatively high surface brightness core regions. Once a source has been detected, an exponential-type source profile will necessarily leak less flux into the background map (beyond its masked detection footprint region) than an equivalent de Vaucouleurs type source, and therefore will contribute less toward background contamination.

We show full recovered background sky maps in Figure 6, visualising each output background model across the entire field. Each panel shows a different recovered background model as a function of software configuration mode (per-row) and simulated data type flavour (per-column). Each pixel in the original 4200 \times 4100 pixel background map has been mean-binned into super-pixels of 100 \times 100 pixels each. Super-pixels are colour-coded according to their equivalent surface brightness value, as shown by the associated colour bar. As such, and for clarity, we show here only the four ‘a’-type full simulated datasets with faint EBL sources included (denlo1a, denlo4a, denhi1a and denhi4a). The spatial trends seen here sync with the global average trends presented above. Background maps derived from high density simulated regions are brighter than their low density counterparts by $\Delta\mu_{\text{hi-lo}} = -0.43$ mag arcsec⁻² on average. Similarly, background maps derived from fields containing highly extended de Vaucouleurs type ($n = 4$) sources are brighter than their exponential ($n = 1$) counterparts by $\Delta\mu_{4-1} = -0.21$ mag arcsec⁻² on average. These global mean offsets again underline the impact of source density and profile type on background modelling, with denser regions and regions comprised of more extended sources notably more affected by sky estimation contaminant flux. Global mean offsets do not tell the whole story however,

with some background models containing a large number of high frequency (small spatial scale) background fluctuations relative to other background models, which remain relatively flat across the field. Such high frequency fluctuations, smaller than the noise level on occasion, are potentially linked to the adopted background mesh size. This is one potential indicator that some configurations are more impacted by singular bright sources than others. In such cases, the detection and measurement of sources may not reach as deep.

Figure 7 shows mean recovered sky levels in units of mag arcsec^{-2} returned by all software configuration modes (see legend) and full ('a'-type) simulated data flavours (per panel). Software packages are uniquely colour coded, with SOURCE EXTRACTOR results in orange, GNUASTRO results in purple, and LSST PIPELINES results in black. Background levels estimated from low density simulated data are shown in the two panels on the left, and their equivalents from high density regions are shown in the two panels on the right. The units along the x axis are arbitrary, to separate out the points. Data points relating to modified, dilated masking and modelled masking are all based upon a default configuration (e.g., the dilated masking procedure is not based upon a modified configuration). Fields populated with exponential ($n = 1$) sources are shown in the uppermost two panels, whilst fields populated with de Vaucouleurs ($n = 4$) type sources are shown in the lower two panels. The global trends discussed above are also evident here, with the field density and profile type acting to modulate the resultant background level by up to half a magnitude. As also shown in Table 1 and Figure 6, Figure 7 additionally acts to highlight the variation in recovered background level as a function of specific software configuration.

4.0.2 Trends by Software Configuration Mode

The faintest sky maps tend to be returned by the modelled masking variant of SOURCE EXTRACTOR, all variants of GNUASTRO, and the S128 variant of the LSST PIPELINES. The most significant improvement over a default configuration mode is the application of modelled masking to SOURCE EXTRACTOR. When this technique is applied, resultant sky maps are fainter than default SOURCE EXTRACTOR by up to an order of magnitude. The model masked SOURCE EXTRACTOR sky map outputs are typically fainter than all other configuration modes in the extended de Vaucouleurs datasets, albeit with a larger scatter, and fainter than all configuration modes other than modified GNUASTRO in the case of exponential datasets. The modelled masking technique is ideally suited to the relatively smaller segmentation masks produced by SOURCE EXTRACTOR. Unlike the dilated masking approach, modelled masking does not reduce the total number of pixels used to estimate the background; a significant benefit in crowded fields. Conversely, out of the box, default SOURCE EXTRACTOR returns some of the brightest sky maps; a well known issue, often encountered in the literature. The modifications made to SOURCE EXTRACTOR do not appear to significantly alter its resultant output sky level relative to its default configuration, although they do act to reduce the scatter. Our primary SOURCE EXTRACTOR modifications are an increase in the background mesh element size (and associated mesh filtering) within which sky

is initially estimated, a reduction in the source detection threshold (i.e., allowing more flux to be classified as signal rather than noise), and changes to the smoothing kernel and segmentation parameters. Many of these changes are often adopted in the literature to improve derived catalogue parameters, yet they appear to have little to no impact on the resultant average sky level. The dilated masking SOURCE EXTRACTOR technique also performs well, notably improving on the average sky level relative to the default results by up to a quarter of a magnitude. This procedure has significant benefits, as explored in Ji et al. (2018), helping reduce contamination at the background estimation step by masking more of the potentially contaminant flux in the wings of bright sources.

Excepting modelled masking, sky recovered by GNUASTRO are of the order half a magnitude fainter than SOURCE EXTRACTOR when comparing like-for-like configuration setups. The consistently faint sky levels returned by GNUASTRO, regardless of configuration mode, are likely attributed to its bottom-up approach towards source identification and characterisation (in contrast to the top-down flux thresholding techniques employed by SOURCE EXTRACTOR and the LSST PIPELINES) and the resultant extensive segmentation maps which leave little room for further modification. The modifications made to GNUASTRO here (an increase in the background mesh size and a reduction in the growth quantile threshold) act to improve the recovered sky map by a quarter of a magnitude, and simultaneously reducing the scatter (i.e., the background maps are less undulating than their default equivalents). The impact of dilated masking and modelled masking relative to default GNUASTRO appears slight. This is likely due to the extensive pixel masks removing additional information from what was, already, a sparse dataset.

The S128 variant of the LSST PIPELINES performs comparably to default GNUASTRO, albeit exhibiting a larger scatter. Conversely, the P6 variant of the LSST PIPELINES typically returns the smallest recovered sky level scatter relative to other software modes explored here, with a typical resultant sky level intermediate to the default outputs given by SOURCE EXTRACTOR and GNUASTRO, and of the order ~ 0.25 mag brighter than S128.

4.0.3 Trends in Output Source Catalogue Fidelity

Whilst the previous sections focus on analysis of the output sky models, the fidelity of the resultant source catalogues is also of interest. To facilitate this analysis we generate a series of matched catalogues for each data output produced here, matching the output catalogue to the known simulated input catalogue using the STILTS¹⁴ software package. We perform a 3-dimensional match between the output and input catalogues based upon x and y pixel coordinates and total magnitude. To match, the output pixel coordinate must be within 5 pixels of its input location (independently on both axes), and the output magnitude must be within 0.5 magnitudes of the input magnitude. Magnitude estimates are derived from the Kron-like FLUX_AUTO value with SOURCE

¹⁴ <http://www.star.bris.ac.uk/~mbt/stilts>

EXTRACTOR outputs, the BRIGHTNESS value with GNUASTRO outputs, and the base_SdssShape_instFlux value with LSST PIPELINES outputs. Figure 8 shows the number of true matched objects (y -axis) as a function of the total number of detected objects (x -axis) for various software configuration modes listed in the legend and simulated data type flavours. Data point type and colour coding is identical to that previously used. Slanted dashed grey lines represent different fidelity fractions in increments of 10%.

We find that SOURCE EXTRACTOR default-based modes of operation (i.e., default, dilated masking and modelled masking) produce the highest fidelity catalogues, with approximately three quarters of output sources finding a corresponding true match in their equivalent original input catalogue. These catalogues also return the fewest total number of objects however, indicating that default SOURCE EXTRACTOR is well optimised towards returning the largest of sources in any given field of view. Modified SOURCE EXTRACTOR operations drastically increase both the total number of output sources (by a factor of ~ 20 on average) and the number of matched sources (by a factor of ~ 6 on average), with a corresponding reduced fidelity ratio of around a quarter.

Default-based GNUASTRO operational modes (i.e., default, dilated masking and modelled masking) similarly cluster together, with a matched fidelity ratio of $\sim 50\%$. These outputs do find a larger number of total sources than their equivalent SOURCE EXTRACTOR runs, however, fewer of these are able to be matched to a known simulated input. Modifications made to GNUASTRO act to somewhat increase the total number of detected objects (by $\sim 10\%$ on average, except in the denlola scenario where a slight decrease is recorded), however, any increase is at the expense of source fidelity, with a drastically reduced recovered fidelity ratio of $\sim 30\%$ or lower.

The two LSST PIPELINES modes of operation perform fairly consistently and comparably to the default GNUASTRO outputs, returning fidelity ratios in the range $\sim 30\%$ to $\sim 60\%$. Simulated regions populated with exponential sources tend to lead to higher fidelity output LSST PIPELINES catalogues on average, with a larger number of spurious sources for no discernible increase in total numbers found in the equivalent de Vaucouleurs populated fields. Progressing from the P6 mode of operation to the S128 variant approximately maintains a similar fidelity level, improving in both total number of detected objects and the equivalent number of true matched sources.

In addition to overall numbers, we also want to explore whether the output magnitudes being returned by our software package of choice accurately portray the true input magnitudes in our simulated datasets. Figure 9 shows median recovered luminosity fractions for the matched source subsets described above. The x -axis shows the median recovered luminosity fraction f for all matched sources, where $f = \text{median}(L_{\text{out}}/L_{\text{in}})$. As L_{in} is a pure simulated input quantity, whereas L_{out} is a measured output quantity, ideal values of f should ideally fall in the range $0 < f < 1$, with higher values preferred. The y -axis represents the median recovered luminosity fraction for the 25 largest matched sources alone (f_{25}). The latter of these two parameters is of particular interest, as these sources have the largest individual impact on background sky estimation results. We

find a strong bimodality in f as a function of source profile type, as might naively be expected, with similar overall trends observed in both regardless of field density.

Here it becomes apparent that SOURCE EXTRACTOR appears optimally configured for the accurate characterisation of exponential type sources, with all SOURCE EXTRACTOR software variants clustering just below $f = 1$ and $f_{25} = 1$, i.e., their median output luminosities accurately represent their inputs. Recovered SOURCE EXTRACTOR results for de Vaucouleurs populated fields are less consistent, with typical median recovered luminosity fractions for de Vaucouleurs type sources in both field density regimes returning $f \sim 0.85$ (and equivalently for the largest 25 sources), i.e., $\sim 15\%$ of their input flux is missing in its output flux estimate. Some flux loss for more extended sources is to be expected, as discussed above, so these results are not too surprising. The value of f varies significantly with SOURCE EXTRACTOR software configuration, with the default mode of operation performing worst, and the modified and modelled masking procedures performing significantly better on average. Several such configuration modes push the SOURCE EXTRACTOR results up to $f \sim 0.95$, however, all continue to struggle for the largest 25 sources.

Conversely, the GNUASTRO package appears designed for the optimal extraction of de Vaucouleurs type sources, more accurately picking up the LSB flux in the wings of these objects. All default-based configuration variants of GNUASTRO return $f \sim 1$ in the case of de Vaucouleurs type simulated datasets. Modified GNUASTRO tends to report an *excess* of flux in de Vaucouleurs type objects by $\sim 5\%$. This is likely due to our choice to lower the detection growth quantile parameter to 0.7 from its default value of 0.9, which improves the sky estimate at the expense of object fidelity. The recovered flux for the 25 largest de Vaucouleurs sources falls somewhat lower, at $f_{25} \sim 0.95$ (i.e., the brightest 25 sources are reported to be $\sim 5\%$ fainter than their input Sérsic magnitude). This in-built facility to identify LSB flux around de Vaucouleurs sources does not similarly lead to a successful outcome in the case of exponential-type populated fields. Recovered exponential source flux appears to be over-estimated by $\sim 10\%$ (and $\sim 15\%$ in the case of a modified GNUASTRO configuration). Unfortunately, it appears that GNUASTRO tends towards inaccurately incorporating flux from surrounding faint EBL sources and noise spikes into these exponential source footprints, falsely inflating their resultant flux estimates above and beyond their known simulated input.

Of all three software packages explored here, results from the LSST PIPELINES consistently recover the lowest flux fractions. In the exponential scenario, recovered fluxes are $\sim 10\%$ lower than their known inputs. When considering the largest 25 sources alone, recovered fluxes are $\sim 15\%$ lower than their known inputs. The situation is notably more extreme in the case of fields populated with de Vaucouleurs sources, with equivalent recovered values of $f \sim 0.8$ and $f_{25} \sim 0.7$, respectively. This potentially indicates that a significant amount of flux from these sources is leaking into the resultant sky estimate, severely contaminating resultant sky maps.

5 CONCLUSIONS

Using a series of simulated images designed to mimic a wide range of Hyper Suprime-Cam Subaru Strategic Program survey data, we examine how varying the galaxy source population, density, and surface brightness profile type influences the background measured across a typical patch of sky. In an era of increasingly deep, wide-area survey science, the potential for LSB discovery is greater than ever before. The potential pitfalls of background over-subtraction on LSB science however is significant (see for example [Aihara et al. 2019](#), Figure 5), with much of this faint flux at severe risk of contamination or destruction during image processing.

This study makes use of three contemporary image processing software packages: SOURCE EXTRACTOR, GNUASTRO, and the LSST SCIENCE PIPELINES. Each package is operated in multiple configuration modes to explore optimal strategies towards recovering a fainter overall background sky, and ones in which low surface brightness features are maximally preserved. Both SOURCE EXTRACTOR and GNUASTRO are operated in four distinct modes: default, modified, with dilated masking, and with modelled masking. The default mode of operation explores how to software performs ‘out-of-the-box’, whilst the modified mode of operation makes a number of changes commonly recommended in the literature which are designed to improve sky estimates and source catalogue fidelity. The dilated masking procedure follows the methodology initially outlined in [Ji et al. \(2018\)](#), whereby the source flux masks are artificially expanded around sources to mask signal flux leakage which would otherwise contaminate the background model. The amount of mask expansion is related to the magnitude of the underlying source. Finally, we present here the modelled masking approach, whereby single-Sérsic parametric models are fit to a subset of detected sources and subtracted. This approach may be considered analogous to a weighted pixel mask technique, whereby an attempt is made to mask only the signal flux out into the noise, rather than using a fixed isophotal threshold mask as with a traditional segmentation map. Following subtraction of the model plane, the sky level is then estimated from the residual image. Finally, the LSST PIPELINES are operated in two distinct modes of operation: a sixth-degree polynomial background mapping approach (P6) and an updated modified 128-pixel spline fitting configuration (S128).

We summarise here our principal conclusions on the nature of background sky estimation as a function of source population parameters and data processing methodology:

1. The faintest and most accurate sky maps are returned when using the modelled masked variant of SOURCE EXTRACTOR, all variants of GNUASTRO, and the S128 variant of the LSST PIPELINES. These software configurations produce sky maps of the order half a magnitude fainter than a default run of SOURCE EXTRACTOR on the same data. The dilated masking variant of SOURCE EXTRACTOR also performs well, returning sky maps of the order a quarter of a magnitude fainter than a default run of SOURCE EXTRACTOR. The apparent success in estimating the sky for techniques which artificially inflate the pixel masks around bright sources is evidence for the significant issue of flux leakage in contaminating background estimation efforts. Should such LSB flux be considered noise, rather than signal, its

chances of being subtracted away in the background model are significant.

2. The ‘top-down’ source extraction software package SOURCE EXTRACTOR identifies a far smaller fraction of pixels in any given field as signal than do the ‘bottom-up’ routines utilised by GNUASTRO. Top-down tools attempt to identify bright source peaks above a limiting isophote, with any flux not successfully detected ultimately entering into the estimate of the background sky. Conversely, the bottom-up routines of GNUASTRO instead attempt to identify contiguous regions of noise, assigning everything else to a detection. In densely packed environments, or fields comprised of more extended sources, bottom-up techniques such as those utilised within GNUASTRO result in most sources being linked by ‘flux-bridges’. Whilst this may have the potential to accurately capture most instances of flux leakage into the background model, this also leaves behind a relatively smaller area of non-signal sky upon which to base a reliable sky model. A key strength of the masked modelling approach when applied to top-down sky estimation techniques such as SOURCE EXTRACTOR is that no additional pixels are required to be masked than would otherwise be by default. This is a crucial consideration for future deep surveys, where the source density will only increase.

3. Adopting optimal source detection configurations for the three software packages given above produces multiple outcomes. Modifications explored here include varying the mesh grid size to be used for determination of the sky level on an image, changing the source detection and analysis thresholds, and modifying the smoothing kernels used to associate regions of noise, amongst others (see text for further details). A negligible change in the mean sky level was found when comparing modified SOURCE EXTRACTOR against its default configuration. Both the GNUASTRO and LSST PIPELINES however recover sky levels up to a quarter of a magnitude fainter than that found previously. We note however that the background map returned by modified SOURCE EXTRACTOR and modified GNUASTRO are notably flatter than that returned by the S128 variant of the LSST PIPELINES, with the latter of these showing distinct background peaks at the position of bright sources. The ideal background map should not display any such peaks, with the presence of these instead indicating that a significant amount of light from singular bright sources has inadvertently leaked through and contaminated the background map estimation.

4. Output source catalogues provided by SOURCE EXTRACTOR tend to recover the fewest total number of sources relative to the other software packages explored here. Of these catalogues however, $\sim 75\%$ of sources can be matched to a known simulated input source. A notable exception is in the case of the modified SOURCE EXTRACTOR configuration, whereby the total number of detections are vastly increased by a factor of ~ 20 yet the number of matches by a factor of only ~ 6 . Output GNUASTRO source catalogues tend to recover slightly more sources than provided by SOURCE EXTRACTOR, yet at the expense of match-to-total ratio¹⁵, with

¹⁵ As noted in Section 3.4.1, here we opt to make use of the *object* catalogues provided by default by the GNUASTRO SEGMENT software. For the data explored here, the associated *clump* catalogue

a reduced fidelity factor of $\sim 50\%$. As with SOURCE EXTRACTOR, modified GNUASTRO catalogues recover a higher total number of sources than by default (excepting in a low density exponential environment) and also exhibit significantly worse fidelity ratios of $\sim 30\%$. Both iterations of the LSST PIPELINES explored here return fidelity ratios of $\sim 50\%$, performing better in high-density exponential type simulated regions, and worse in low-density de Vaucouleurs type fields. Switching from the P6 variant to the S128 variant approximately maintains the fidelity ratio whilst increasing the total number of detections. These results suggest that top-down tools such as SOURCE EXTRACTOR have been designed with the detection of the brightest of sources in mind, resulting in a reduction in the number of false positives than would otherwise be returned.

5. The SOURCE EXTRACTOR routines successfully capture almost all of the light associated with exponential type simulated sources, in both high and low density environments. Exponential source fluxes output by default SOURCE EXTRACTOR modes of operation return $\sim 95\%$ of the known input flux. This rises up to $\sim 100\%$ of the known input flux being correctly identified in the case of SOURCE EXTRACTOR with modelled masking. For de Vaucouleurs type galaxies, default SOURCE EXTRACTOR returns a lower recovered luminosity fraction of $\sim 80\%$ (i.e., $\sim 20\%$ of the known input light is missing), rising to $\sim 90\%$ in the case of SOURCE EXTRACTOR with modelled masks and higher still when utilising a modified configuration. From this we deduce that SOURCE EXTRACTOR appears optimally configured for the detection of more compact sources, with modifications or the application of modelled masking required to perform equivalently with more extended sources.

6. The GNUASTRO routines successfully capture almost all of the light associated with extended de Vaucouleurs type sources, in both high and low density environments. Output fluxes for de Vaucouleurs sources are within a few percent

(the high signal-to-noise cores of the brightest sources) tends to return far fewer sources. For example, for the *denhi4b* simulated dataset, the default output GNUASTRO catalogue contains 3720 clumps and 5261 objects. This is caused by some ‘signal’ pixel regions not containing any significant flux peak to constitute a clump. Furthermore, some clumps are merged into a single object because the maximum value of the signal-to-noise in the ‘river’ pixels between two clumps falls below the default value of 1 (a value which may be over-ridden by the SEGMENT parameter *objbordersn*). Utilising a clump catalogue instead of an object catalogue may well return a higher match-to-total ratio, however, the clump catalogue by definition does not encompass all non-noise pixels detected in an image. Conversely, the object catalogue is directly related to those pixels which were not found to be noise (information which is used to assist in sky estimation), therefore making it the more appropriate choice for our further analysis in this paper. It is tempting to consider making use of a modified object catalogue, setting *objbordersn* to some very high value (i.e., never merging multiple clumps together into one object). This would have the advantage of returning the maximum number of objects at the expense of never merging together clumps which are sub-components of a single object, as is the case with, for example, a star-forming knot within an extended source. As some form of clump merging will always be required in real data analysis, we do not consider this a viable approach to further explore in this study.

of their known input flux, with the exception of GNUASTRO operating in a modified configuration which results in an overestimation of the source flux by $\sim 5\%$. In the case of exponential simulated inputs, GNUASTRO tends to overestimate the measure of flux by $\sim 10\%$, excepting GNUASTRO operating in a modified configuration whereby flux estimates are $\sim 15\%$ brighter than their known inputs. This tendency for recovered exponential flux estimates to be $\sim 10\%$ brighter than their known simulated input is a serious cause for concern, implying that a significant amount of contaminant flux is being included at the source detection phase. As GNUASTRO has a wide range of configuration parameters, further such modifications in addition to those tested here should be sought out to attempt to mitigate this undesirable effect.

7. Both variants of the LSST PIPELINES tested here recover somewhat lower flux fractions than had been initially input. In the case of exponential type sources, the LSST PIPELINES recover $\sim 90\%$ of the input light. This reduces to $\sim 75\%$ of the input light in the case of de Vaucouleurs type sources. Slight $\sim \text{few}\%$ improvements are noted when switching from the P6 to the S128 variant, in both high and low density environments. As the top-down sky estimation and source extraction philosophies behind SOURCE EXTRACTOR and the LSST PIPELINES are similar in nature, it is likely that application of either the dilated masking procedure or the modelled masking approach would have a similarly beneficial effect.

8. The faint extragalactic background light (EBL) component, largely associated with undetectable sources, plays a significant role in modifying the overall recovered sky level pedestal. Simulated fields containing an EBL component are brighter in the range $1.8 \leq \sigma \leq 39.5$ than an equivalent field with the EBL component removed, with an average of 8.3σ brighter. As such sources are ubiquitous, their impact on local background estimation is simpler to predict at present. Future surveys probing to deeper depths may ultimately require a more considered approach towards characterising such a component.

9. The recovered background sky is considerably biased bright in regions of high source density relative to less densely packed fields. Simulated high density environments return a background sky brighter than their low density equivalents in the range $1.1 \leq \sigma \leq 15.2$; 3.3σ on average. The additional flux thrown out into the background map by these extra sources acts to notably contaminate sky estimation routines, with denser regions more severely impacted. This is an important consideration for analysis of clustered environments, and an increasingly important consideration for future deep surveys such as the LSST.

10. Regions of sky containing extended de Vaucouleurs type galaxies are more difficult to derive an accurate background estimate for than regions populated with less extensive exponential type sources. Of these two types, fields containing de Vaucouleurs sources return sky estimates that are brighter than those equivalents from fields containing exponential sources in the range $0.0 \leq \sigma \leq 11.8$, with an average significance of 2.4σ brighter. The de Vaucouleurs surface brightness profile, often associated with spheroidal elliptical galaxies, throws out significantly more flux into its wings than does an exponential profile. Other sources with bright extended wings, such as the extended halo of a PSF, also have the potential for a significant fraction of their light

to be left undetected and unaccounted for beneath the limiting isophote, further contributing to background sky estimate contamination. These results highlight the importance for future optimal LSB detection strategies to be sensitive to the form of the bright sources they neighbour.

The choice of software package and its configuration is based on the specific science question one wishes to answer. In the case of LSB science, the ability to recover a faint and flat sky is paramount. Of the software types and configurations tested here, the results of this study suggest that the faintest and most reliable sky maps are recovered when the modelled masking technique is applied to data processed by SOURCE EXTRACTOR, producing the largest average sky level improvements of any technique tested herein. The distinct advantage of this approach is that it requires significantly smaller detection footprints to operate successfully, with the dual bonus advantages of a lower false-positive detection rate and the tendency not to over-estimate source flux in output source catalogues. The top-down approaches of SOURCE EXTRACTOR and the LSST PIPELINES seemingly lend themselves to a greater range of configurational possibility. Conversely, bottom-up source detection routines as utilised by GNUASTRO also return faint sky maps, however, at the expense of masking a much larger fraction of the field of view. Such a philosophy may not be sustainable as we enter an era of increasingly deep, wide-area survey science, wherein rising source densities will make it harder to find ‘empty’ patches of sky from which to derive a background model. The accuracy of output background sky models are found to vary as a function of source population, density, and type, with different considerations to be made in the case of each. Subsequent modifications to contemporary image processing pipelines such as the the Rubin Observatory LSST SCIENCE PIPELINES which address these concerns would therefore be of significant benefit, not only to the LSB science community, but to the entire scientific user base as a whole.

ACKNOWLEDGEMENTS

We thank Robert Armstrong, Eli Rykoff and Jeff Carlin for their significant and helpful comments on earlier drafts of this paper. This material is based upon work supported in part by the National Science Foundation (NSF) through Cooperative Agreement 1258333 managed by the Association of Universities for Research in Astronomy (AURA), and the Department of Energy under Contract No. DE-AC02-76SF00515 with the SLAC National Accelerator Laboratory. Additional funding for Rubin Observatory comes from private donations, grants to universities, and in-kind support from LSSTC Institutional Members. This research was also supported by Department of Energy grant DE-SC0009999 and NSF/AURA grant N56981C.

The Hyper Suprime-Cam (HSC) collaboration includes the astronomical communities of Japan and Taiwan, and Princeton University. The HSC instrumentation and software were developed by the National Astronomical Observatory of Japan (NAOJ), the Kavli Institute for the Physics and Mathematics of the Universe (Kavli IPMU), the University of Tokyo, the High Energy Accelerator Research Organization (KEK), the Academia Sinica Institute for Astronomy and Astrophysics in Taiwan (ASIAA), and Princeton University. Funding was contributed by the FIRST program from Japanese Cabinet Office, the Ministry of Education, Culture, Sports, Science and Technology (MEXT), the Japan Society for the Promotion of Science (JSPS), Japan Science and Technology Agency (JST), the Toray Science Foundation, NAOJ, Kavli IPMU, KEK, ASIAA, and Princeton University.

This paper makes use of software developed for the Large Synoptic Survey Telescope. We thank the LSST Project for making their code available as free software at <http://dm.lsst.org>.

The Pan-STARRS1 Surveys (PS1) have been made possible through contributions of the Institute for Astronomy, the University of Hawaii, the Pan-STARRS Project Office, the Max-Planck Society and its participating institutes, the Max Planck Institute for Astronomy, Heidelberg and the Max Planck Institute for Extraterrestrial Physics, Garching, The Johns Hopkins University, Durham University, the University of Edinburgh, Queen’s University Belfast, the Harvard-Smithsonian Center for Astrophysics, the Las Cumbres Observatory Global Telescope Network Incorporated, the National Central University of Taiwan, the Space Telescope Science Institute, the National Aeronautics and Space Administration under Grant No. NNX08AR22G issued through the Planetary Science Division of the NASA Science Mission Directorate, the National Science Foundation under Grant No. AST-1238877, the University of Maryland, and Eotvos Lorand University (ELTE) and the Los Alamos National Laboratory.

This work was partly done using GNU Astronomy Utilities (Gnuastro, ascl.net/1801.009) version 0.17. Work on Gnuastro has been funded by the Japanese Ministry of Education, Culture, Sports, Science, and Technology (MEXT) scholarship and its Grant-in-Aid for Scientific Research (21244012, 24253003), the European Research Council (ERC) advanced grant 339659-MUSICOS, European Union’s Horizon 2020 research and innovation programme under Marie Skłodowska-Curie grant agreement No 721463

to the SUNDIAL ITN, and from the Spanish Ministry of Economy and Competitiveness (MINECO) under grant number AYA2016-76219-P.

DATA AVAILABILITY

All data and associated code produced for use within this study has been archived on the ZENODO open-access repository at <https://doi.org/10.5281/zenodo.7067465>.

REFERENCES

- Aihara H., et al., 2011, *ApJS*, **193**, 29
- Aihara H., et al., 2018a, *PASJ*, **70**, S4
- Aihara H., et al., 2018b, *PASJ*, **70**, S8
- Aihara H., et al., 2019, *PASJ*, **71**, 114
- Akhlaghi M., 2019, arXiv e-prints, p. [arXiv:1909.11230](https://arxiv.org/abs/1909.11230)
- Akhlaghi M., Ichikawa T., 2015, *ApJS*, **220**, 1
- Arp H., 1965, *ApJ*, **142**, 402
- Baldry I. K., Glazebrook K., Brinkmann J., Ivezić Ž., Lupton R. H., Nichol R. C., Szalay A. S., 2004, *ApJ*, **600**, 681
- Baldry I. K., Balogh M. L., Bower R. G., Glazebrook K., Nichol R. C., Bamford S. P., Budavari T., 2006, *MNRAS*, **373**, 469
- Barden M., Häußler B., Peng C. Y., McIntosh D. H., Guo Y., 2012, *MNRAS*, **422**, 449
- Bauer A. E., et al., 2013, *MNRAS*, **434**, 209
- Bertin E., 2011, in Evans I. N., Accomazzi A., Mink D. J., Rots A. H., eds, *Astronomical Society of the Pacific Conference Series Vol. 442, Astronomical Data Analysis Software and Systems XX*. p. 435
- Bertin E., Arnouts S., 1996, *A&AS*, **117**, 393
- Binggeli B., Sandage A., Tammann G. A., 1988, *ARA&A*, **26**, 509
- Blanton M. R., Kazin E., Muna D., Weaver B. A., Price-Whelan A., 2011, *AJ*, **142**, 31
- Bosch J., et al., 2018, *PASJ*, **70**, S5
- Bosch J., et al., 2019, in Teuben P. J., Pound M. W., Thomas B. A., Warner E. M., eds, *Astronomical Society of the Pacific Conference Series Vol. 523, Astronomical Data Analysis Software and Systems XXVII*. p. 521 ([arXiv:1812.03248](https://arxiv.org/abs/1812.03248))
- Brough S., et al., 2011, *MNRAS*, **413**, 1236
- Caon N., Capaccioli M., D’Onofrio M., 1993, *MNRAS*, **265**, 1013
- Cardamone C., et al., 2009, *MNRAS*, **399**, 1191
- Chambers J. M., Hastie T. J., 1992, *Statistical models in S*. Chapman and Hall/CRC
- Cheselka M., 1999, in Mehringer D. M., Plante R. L., Roberts D. A., eds, *Astronomical Society of the Pacific Conference Series Vol. 172, Astronomical Data Analysis Software and Systems VIII*. p. 349
- D’Souza R., Kauffman G., Wang J., Vegetti S., 2014, *MNRAS*, **443**, 1433
- Desai S., Mohr J. J., Bertin E., Kümmel M., Wetzstein M., 2016, *Astronomy and Computing*, **16**, 67
- Driver S. P., et al., 2006, *MNRAS*, **368**, 414
- Fixsen D. J., Offenberg J. D., Hanisch R. J., Mather J. C., Nieto-Santisteban M. A., Sengupta R., Stockman H. S., 2000, *PASP*, **112**, 1350
- Garstang R. H., 1989, *PASP*, **101**, 306
- Goldstein D. A., et al., 2015, *AJ*, **150**, 82
- Graham A. W., Driver S. P., 2005, *Publ. Astron. Soc. Australia*, **22**, 118
- Guzmán R., Gallego J., Koo D. C., Phillips A. C., Lowenthal J. D., Faber S. M., Illingworth G. D., Vogt N. P., 1997, *ApJ*, **489**, 559
- Häußler B., et al., 2007, *ApJS*, **172**, 615
- Häußler B., et al., 2013, *MNRAS*, **430**, 330
- Hiemer A., Barden M., Kelvin L. S., Häußler B., Schindler S., 2014, *MNRAS*, **444**, 3089
- Hill D. T., et al., 2011, *MNRAS*, **412**, 765
- Huang S., et al., 2018, *PASJ*, **70**, S6
- Iodice E., et al., 2016, *ApJ*, **820**, 42
- Ivezić Z., et al., 2008, *Serbian Astronomical Journal*, **176**, 1
- Ivezić Ž., et al., 2019, *ApJ*, **873**, 111
- Jarvis J. F., Tyson J. A., 1981, *AJ*, **86**, 476
- Ji I., Hasan I., Schmidt S. J., Tyson J. A., 2018, *PASP*, **130**, 084504
- Jurić M., et al., 2017, in Lorente N. P. F., Shortridge K., Wayth R., eds, *Astronomical Society of the Pacific Conference Series Vol. 512, Astronomical Data Analysis Software and Systems XXV*. p. 279 ([arXiv:1512.07914](https://arxiv.org/abs/1512.07914))
- Karabal E., Duc P. A., Kuntschner H., Chanial P., Cuillandre J. C., Gwyn S., 2017, *A&A*, **601**, A86
- Kelvin L., Driver S., Robotham A., Hill D., Cameron E., 2010, in Debattista V. P., Popescu C. C., eds, *American Institute of Physics Conference Series Vol. 1240, Hunting for the Dark: the Hidden Side of Galaxy Formation*. pp 247–248, [doi:10.1063/1.3458501](https://doi.org/10.1063/1.3458501)
- Kelvin L. S., et al., 2012, *MNRAS*, **421**, 1007
- Kelvin L. S., et al., 2014a, *MNRAS*, **439**, 1245
- Kelvin L. S., et al., 2014b, *MNRAS*, **444**, 1647
- Kelvin L. S., et al., 2018, *MNRAS*, **477**, 4116
- Knapen J. H., Trujillo I., 2017, *Ultra-Deep Imaging: Structure of Disks and Haloes*. Springer, p. 255, [doi:10.1007/978-3-319-56570-5_8](https://doi.org/10.1007/978-3-319-56570-5_8)
- Lupton R., Gunn J. E., Ivezić Z., Knapp G. R., Kent S., 2001, in Harnden F. R. J., Primini F. A., Payne H. E., eds, *Astronomical Society of the Pacific Conference Series Vol. 238, Astronomical Data Analysis Software and Systems X*. p. 269 ([arXiv:astro-ph/0101420](https://arxiv.org/abs/astro-ph/0101420))
- Miyazaki S., et al., 2012, in McLean I. S., Ramsay S. K., Takami H., eds, *Society of Photo-Optical Instrumentation Engineers (SPIE) Conference Series Vol. 8446, Ground-based and Airborne Instrumentation for Astronomy IV*. p. 84460Z, [doi:10.1117/12.926844](https://doi.org/10.1117/12.926844)
- Miyazaki S., et al., 2018, *PASJ*, **70**, S1
- Montes M., Trujillo I., 2014, *ApJ*, **794**, 137
- Montes M., Trujillo I., 2018, *MNRAS*, **474**, 917
- Montes M., Trujillo I., 2019, *MNRAS*, **482**, 2838
- Pence W. D., Seaman R., White R. L., 2009, *PASP*, **121**, 414
- Pence W. D., White R. L., Seaman R., 2010, *PASP*, **122**, 1065
- R Core Team 2020, *R: A Language and Environment for Statistical Computing*. R Foundation for Statistical Computing, Vienna, Austria, <https://www.R-project.org/>
- Ripley B. D., 1987, *Stochastic Simulation*. Wiley, <https://www.wiley.com/en-us/Stochastic+Simulation-p-9780470009604>
- Robotham A. S. G., Davies L. J. M., Driver S. P., Koushan S., Taranu D. S., Casura S., Liske J., 2018, *MNRAS*, **476**, 3137
- Rowe B. T. P., et al., 2015, *Astronomy and Computing*, **10**, 121
- Sandage A., Binggeli B., 1984, *AJ*, **89**, 919
- Sérsic J. L., 1963, *Boletín de la Asociación Argentina de Astronomía La Plata Argentina*, **6**, 41
- Sérsic J. L., 1968, *Atlas de Galaxias Australes*. Observatorio Astronómico, Universidad Nacional de Córdoba
- Simard L., Mendel J. T., Patton D. R., Ellison S. L., McConnachie A. W., 2011, *ApJS*, **196**, 11
- Sreejith S., et al., 2018, *MNRAS*, **474**, 5232
- Stinson G. S., Dalcanton J. J., Quinn T., Kaufmann T., Wadsley J., 2007, *ApJ*, **667**, 170
- Storkey A. J., Hambly N. C., Williams C. K. I., Mann R. G., 2004, *MNRAS*, **347**, 36
- Taylor E. N., et al., 2015, *MNRAS*, **446**, 2144
- Teeninga P., Moschini U., Trager S. C., Wilkinson M. H., 2015, in *International Symposium on Mathematical Morphology and*

- Its Applications to Signal and Image Processing. pp 157–168
 Trujillo I., Fliri J., 2016, *ApJ*, **823**, 123
 Trujillo I., Erwin P., Asensio Ramos A., Graham A. W., 2004, *AJ*, **127**, 1917
 Turner S., et al., 2019, *MNRAS*, **482**, 126
 Vandame B., 2001, in Banday A. J., Zaroubi S., Bartelmann M., eds, Mining the Sky. p. 595, doi:10.1007/10849171_78
 Wang W., et al., 2019, *MNRAS*, **487**, 1580
 Williams R. P., et al., 2016, *MNRAS*, **463**, 2746
 van Dokkum P. G., Abraham R., Merritt A., Zhang J., Geha M., Conroy C., 2015, *ApJ*, **798**, L45
 van der Burg R. F. J., Muzzin A., Hoekstra H., 2016, *A&A*, **590**, A20

APPENDIX A: THE HYPER SUPRIME-CAM SUBARU STRATEGIC PROGRAM

To ascertain the veracity of any given sky subtraction methodology, a real-world observed dataset is required upon which to base a subsequent series of complex simulations. To fill this role, we opt for data taken from the Hyper Suprime-Cam (HSC, Miyazaki et al. 2012, 2018) Subaru Strategic Program (SSP, Aihara et al. 2018a). The HSC is an 870 megapixel prime focus camera consisting of 116 $2k \times 4k$ 0.168 arcsec/pixel CCDs mounted on the 8.2m Subaru telescope at Mauna Kea in Hawaii. HSC-SSP survey data is segregated into three distinct layers: Wide (1400 deg^2), Deep (27 deg^2) and UltraDeep (3.5 deg^2), the former of which is utilised here. Wide-layer optical imaging is provided in the g , r , i , z and y broad-band filters, with a typical 5σ point source depth of $r \sim 26$ mag. Unless otherwise stated, primary analyses throughout the remainder of this study are based upon HSC-SSP r -band data.

The HSC-SSP Public Data Release 1 (PDR1¹⁶, Aihara et al. 2018b) dataset used in this study spans $\sim 100 \text{ deg}^2$ from the initial 12 month observing period, providing full-depth, reduced, calibrated imaging and relevant associated catalogue data. PDR1 full-depth co-added imaging is stored in a hierarchical format. Top level 2.82 deg^2 ‘tracts’ are organised to efficiently tile across the entire survey region, with each tract further subdivided into 9×9 slightly overlapping ‘patches’ of 0.038 deg^2 . HSC-SSP PDR1 imaging data is processed using the HSCPIPE 4 pipeline (Bosch et al. 2018; Huang et al. 2018); an HSC-specific customisation of the Rubin Observatory (formerly Large Synoptic Survey Telescope, Ivezić et al. 2008) LSST SCIENCE PIPELINES Data Management (DM) software stack (Jurić et al. 2017), which itself is based upon concepts initially developed for use within the Sloan Digital Sky Survey (SDSS) Photo pipeline (Lupton et al. 2001). The HSCPIPE 4 pipeline is tasked with a number of processing steps, summarised briefly here: initial raw data acquisition; single-visit CCD image calibration (e.g., bad pixel mask, bias correction, flat-fielding); sky estimation; PSF generation; source extraction, segmentation and deblending; pixel resampling, and; image co-addition. Full details of this processing pipeline, notably the sky estimation methodology, can be found in Bosch et al. (2018) and references therein. The significant depth, multi-wavelength aspect, wide area coverage, and data-processing synergies

with prior and future imaging surveys make the HSC-SSP an ideal candidate for further exploration of contemporary sky-subtraction algorithms. We note that a subsequent data release has occurred since the primary analyses within this paper were conducted. Whilst improvements have been made (see Aihara et al. 2019, Figure 5), the underlying effects explored in this paper remain valid here and for other comparable surveys.

A1 High/Low Density Sample Regions

It is fair to assume that sky estimation routines perform differently in regions of differing source density. To that end, we require two sample regions upon which to base our subsequent simulations: one of relatively low source density and one of relatively high source density. A pseudo-random list of 57 unique tract-patch pairs¹⁷ is generated from the HSC-SSP PDR1 dataset, providing an unbiased sample of HSC imaging data across a wide area. The r -band coadded calibrated exposure (`deepCoadd_calExp`) data products containing the HSCPIPE 4 background-subtracted science images, pixel masks and variance maps are downloaded for each of these tract-patch pairs.

In order to provide an initial estimate of field density for each tract-patch region, the SOURCE EXTRACTOR (Bertin & Arnouts 1996) source detection software package (version 2.25.3) is applied to each science image. The SOURCE EXTRACTOR package is operated using mostly the default configuration setup¹⁸, with the exception of detection threshold which is fixed to an absolute value of 0.07 counts¹⁹. The default operation of SOURCE EXTRACTOR defines sources as those with significant flux above a 1.5σ background threshold. Maintaining such a relative threshold across each tract-patch pair would introduce a sky estimation dependency on source density, and unfairly bias against regions where the initial estimation of the background is inaccurate. Preliminary testing of our dataset found that an absolute threshold of 0.07 counts is sufficient to provide an unbiased estimate of source density for each tract-patch pair in these data. See Section C for more information on the derivation of this absolute detection threshold level. Using this absolute detection threshold, SOURCE EXTRACTOR is once again ran on all 57 tract-patch regions, generating an estimate of field density (number of objects per square arcminute) in addition to a host of per-object parameters particular to each detected object²⁰.

¹⁷ All 57 tract-patch pairs: 8279-07, 8280-18, 8281-28, 8282-37, 8283-38, 8284-47, 8285-27, 8520-03, 8521-46, 8522-50, 8523-51, 8524-52, 8525-53, 8526-21, 8762-00, 8763-14, 8764-15, 8765-22, 8766-23, 8767-24, 8768-61, 9314-08, 9315-48, 9316-57, 9317-58, 9318-17, 9346-16, 9347-41, 9348-42, 9349-26, 9370-02, 9371-36, 9372-43, 9373-44, 9374-45, 9375-31, 9557-06, 9558-55, 9559-56, 9560-62, 9561-40, 9562-54, 9589-05, 9590-32, 9591-33, 9592-20, 9613-01, 9614-30, 9615-34, 9616-35, 9617-25, 9618-60, 9800-04, 9801-11, 9802-12, 9803-13, 9804-10.

¹⁸ Default SOURCE EXTRACTOR configuration file and parameter lists are generated on the command line using the arguments `-dd` and `-dp`, respectively. Default SOURCE EXTRACTOR neural network and convolution files are provided with the software.

¹⁹ Using the standard HSC-SSP flux to nanoJansky conversion factor, 0.07 counts corresponds to $\sim 4 \text{ nJy}$.

²⁰ Our output SOURCE EXTRACTOR catalogue parameters

¹⁶ <https://hsc-release.mtk.nao.ac.jp>

Recovered field densities for all tract-patch regions are shown in Figure A1. Values range from ~ 40 to ~ 100 objects per square arcminute (~ 150000 to ~ 350000 objects per square degree). To select two sample fields, we exclude outliers at both the extreme low density and high density terminus of this range, and select the tract-patch regions located at the 5th and 95th percentiles of recovered field density. The fields found at these percentiles are used as the bases for our low and high density regions, respectively. Tract-patch 8283-38 represents our low density region, containing 6813 detected objects ($\sim 45 N_{\text{obj}} / \text{arcmin}^2$ or $\sim 181991 N_{\text{obj}} / \text{sq. deg.}$), whilst tract-patch 9592-20 represents our high density region, containing 12183 detected objects ($\sim 90 N_{\text{obj}} / \text{arcmin}^2$ or $\sim 325435 N_{\text{obj}} / \text{sq. deg.}$).

Postage stamps and associated segmentation maps for the low density (tract-patch 8283-38) and high density (tract-patch 9592-20) regions can be found in Figures A2 and A3, respectively (see captions for further details). As can be seen, the relatively high resolution and depth of the HSC dataset make these data an ideal candidate for further exploration of sky-subtraction methodologies. Several imaging artefacts remain in these data in addition to the obvious sky over-subtraction impact, notably, central saturation and diffraction spikes associated with bright point sources, optical ghosts, and shredding of bright objects. Whilst these artefacts do not severely impact our subsequent analyses, we highlight them here for reference.

A2 Point Spread Function

It is necessary to convolve our simulated images with a realistic point spread function (PSF) in order to fully account for the impact of the imaging system upon the data. We opt to generate a model of the PSF in the low density region (tract-patch 8283-38) and utilise the resultant PSF model for all subsequent simulated imaging. We use the PSFEX (Bertin 2011) PSF extraction software package (version 3.17.1) to generate an empirical PSF from an input SOURCE EXTRACTOR catalogue. The SOURCE EXTRACTOR software is operated in a similar manner to that outlined in Section A1, with the exception that the output catalogue type must be in the FITS Leiden Data Analysis Center (LDAC) file format. This file format allows for more complex data and imaging to be stored in a single entity, facilitating later PSF extraction. The columns output in this catalogue must contain: VIGNET(101,101); X_IMAGE; Y_IMAGE; FLUX_RADIUS; SNR_WIN; FLUX_APER(1); FLUXERR_APER(1); ELONGATION; and FLAGS. The numbers inside parenthesis following VIGNET specify the postage stamp pixel cutout size around each input point source which will ultimately be used to help define the PSF. A full description of the remaining parameters can be found in Bertin (2011), and references therein. The resultant catalogue is used as an input to PSFEX. As with SOURCE EXTRACTOR, PSFEX is largely operated using its in-built de-

are: NUMBER, FLUX_AUTO, MAG_AUTO, KRON_RADIUS, PETRO_RADIUS, BACKGROUND, THRESHOLD, X_IMAGE, Y_IMAGE, A_IMAGE, B_IMAGE, THETA_IMAGE, ELLIPTICITY, CLASS_STAR and FLUX_RADIUS. A full description of each parameter may be found in Bertin & Arnouts (1996).

faults. Sources identified as point-source-like are added to a library. From our 101×101 pixel vignettes, we request a single output snapshot PSF of size 55×55 pixels in dimension.

The PSFEX outputs are shown in Figure A4. The top panel shows a random selection of 27 out of a total of 424 point sources used to construct this PSF. Nearby neighbours which may act as a flux contaminant are automatically masked prior to use. The shape and position of these point sources on the original frame are used to construct a 2^{nd} -order polynomial model of the PSF, which is shown in the middle-left panel. This model exhibits good circular symmetry, with a measured ellipticity of $e = 1 - b/a \approx 0.04$. Contaminant noise does become increasingly evident in the wings, however, the goodness of fit $\chi^2/\nu = 0.99$ indicates a good match between the model and the input data. The empirical full-width at half-maximum is found to be $\Gamma = 0.72$ arcsec. As shown in the middle-right panel, the PSF closely approximates a Moffat function down to very faint magnitudes, with fitted parameters and confidence intervals given in the inset legend. The result of subtracting a scaled version of the PSF to each of the input point source samples is shown in the lower panel. The majority of point source flux is removed in the residual frame, again evidencing the high-fidelity nature of our output PSF. This PSF is used for all subsequent relevant data analysis.

APPENDIX B: GalSim SIMULATIONS

GALSIM (Rowe et al. 2015) is an open source software package designed to produce highly accurate simulated astronomical imaging. It has a number of powerful capabilities, including the ability to generate a broad range of galaxy and stellar profile types, perform rapid and accurate PSF convolution, and apply a physically motivated noise model. For these reasons, in addition to the speed and accuracy of the underlying base code, we opt to use the GALSIM package (version 2.2.6) to generate our simulated imaging.

Prior to running the GALSIM software, input catalogues and associated YAML configuration files must be generated to specify all necessary simulation parameters. Here we generate realistic simulated regions with noise approximating that found in HSC-SSP PDR1 data and populated with a range of objects exhibiting features similar to those found in our chosen low-density and high-density HSC-SSP PDR1 regions. Each region is exactly 4200×4100 pixels in dimension (approximately $706'' \times 689''$). As a caveat, and for the sake of simplicity, we opt to populate these regions with extended-type Sérsic (1963, 1968) profiles alone, avoiding the additional complication of point sources which typically contribute less to sky estimation errors (excepting the extreme bright-end population of stars) than extended profiles. Each Sérsic profile requires a total of eight input parameters: pixel position in both x and y ; total luminosity in counts; half-light radii in pixels; an axis ratio (i.e., $q = 1 - e = b/a$); a position angle in degrees; a Sérsic index n , and; a postage stamp size in pixels. The latter of these parameters provides the edge size of a square stamp on which to draw the objects within GALSIM²¹.

²¹ Postage stamp size is not strictly required in order to generate a Sérsic profile when using GALSIM, with a default option avail-

Input catalogues must mimic the distribution of features in the sample regions as closely as possible. A number of objects will however be missing from any detection catalogue, owing to either bright-end confusion or faint-end incompleteness. Some such parameters for these extrapolated objects require a meaningful estimation, whilst others require explicit definition. In the following sections, we provide an overview of the derivation of each required simulation parameter, concluding with a summary of our simulated field data generation.

B1 Number Counts & Magnitudes

Perhaps the most fundamental parameter required to populate any simulated input catalogue is how many objects overall one wishes to simulate as a function of magnitude. As an initial guide, we have input catalogues for both sample regions from our initial SOURCE EXTRACTOR runs. The solid emboldened lines in Figure 2 show the detected number of sources per square degree and per magnitude as a function of apparent r -band magnitude, using a histogram bin width of $\Delta m_r = 0.5$ mag. The low density region shown in the left panel, tract-patch 8283-38, contains a total of 6813 detected sources. The high density region shown in the right panel, tract-patch 9592-20, contains a total of 12183 detected sources. The dotted horizontal line in both panels represents the number density corresponding to one object per the area of a sample field (~ 0.038 deg²) per magnitude.

The brightest detected sources are found at $m_r \sim 15.5$ mag in the low density region and $m_r \sim 17$ mag in the high-density region. Number densities then rise in a somewhat stochastic nature down to $m_r \sim 22$ mag in both fields. The fluctuations in source number density as a function of magnitude are as expected, owing to the aforementioned bright-end source confusion. In this regime, it is common for bright sources to become shredded, or for the flux in their wings to become erroneously attributed to or separated from a neighbouring source.

The source density profile continues to rise in the magnitude range $22 < m_r < 25$ mag (represented by two vertical dashed lines) in a log-linear fashion. A constrained log-linear fit to the detected source density profile in this regime is represented as a solid thin line in both panels. Following Ji et al. (2018), the slope of this best fit line is kept fixed, with only the intercept parameter fitted. We find the low density regime source density profile goes as $\log_{10} N_{\text{obj}} = -5.07 + 0.4m_r$. The high density regime source density profile goes as $\log_{10} N_{\text{obj}} = -4.90 + 0.4m_r$.

At magnitudes fainter than $m_r \sim 25$ mag, detected source densities begin to turn down, dropping off completely by $m_r \sim 28$ mag. Such faint-end incompleteness is inherent in any source detection catalogue, as sources gradually become indistinguishable from the background noise and instead contribute to the faint undetected EBL.

Detected sources brighter than $m_r = 22$ mag are significantly more numerous than that predicted by our best fit log-linear trend line, occasionally by almost an order of magnitude. It would be unwise to use these catalogue entries

able. However, for reasons further described below, we require that this parameter be specified here.

when defining a simulated input catalogue if indeed these sources are erroneously shredded sub-components of larger singular sources. For the purposes of defining a simulated catalogue, we opt to discard all detected sources brighter than $m_r = 22$ mag and use the best fit trend line to define a replacement bright end dataset in its place. New bright mock sources are distributed uniformly within each $\Delta m_r = 0.5$ mag bin. This procedure produces a total of 272 new sources in the low density region and 405 new sources in the high density region.

Remaining detected sources at intermediate and faint magnitudes are relatively free from such source processing issues. A single object detected in the low density region exhibited an erroneous flux value, and is consequently removed from all subsequent analyses. We therefore opt to propagate 6325 such objects through to our simulated input catalogue from the low density region, and 11572 from the high density region.

To account for known faint end incompleteness, we additionally derive a population of faint missing sources in the range $25 < m_r < 30$ mag. These sources are defined as the population required in addition to any detected and used sources which would satisfy our best-fit log-linear source density trend line. As with the bright mock sources, these new faint sources are distributed uniformly in magnitude space within each $\Delta m_r = 0.5$ mag bin. As such, this provides an additional 421660 faint end sources in the low density region, and 624238 faint end sources in the high density region.

In summary, we define three distinct flux-associated source populations: bright mock sources, intermediate-brightness detected and used sources, and faint missing sources. These three populations are propagated through to our simulated catalogue and are represented in Figure 2 as dark grey, hatched, and light grey shaded regions, respectively. In total, we simulate 428257 sources in the low density regime and 636215 sources in the high density regime. Magnitudes are converted to flux counts for injection using the standard HSC-SSP `deepCoadd_calexp` zero point magnitude of 27.0 mag ADU^{-1} (Aihara et al. 2018b).

B2 Half Light Radii

It's necessary and desirable for our simulated source sizes to mimic as closely as possible the distribution of size as a function of magnitude found in our observed data. The preliminary source detection catalogues provide half light radii (`FLUX_RADIUS`) for our chosen intermediate brightness detected & used sources; a starting point upon which to generate an appropriate size-magnitude distribution. Some form of extrapolation is however required to provide radii for the remaining brighter/fainter simulated source populations as outlined in Section B1.

Figure B1 shows recovered half light radii as a function of apparent r -band magnitude for all extended-type detected sources in both the low-density region (orange data points) and high-density region (purple data points). We define extended-type sources as those with a SOURCE EXTRACTOR stellar classification parameter in the range `CLASS_STAR` < 0.05 , removing obvious point sources. The application of this cut removes 386 of 18995 potential sources. Despite making this cut, two remnant point source spurs are evident at

$r_{e,\text{low}} \approx 0.5$ and $r_{e,\text{high}} \approx 0.3$, with the low density region PSF evidently more extended than its high density region equivalent. The apparent bias in half light radius at any given magnitude as a function of field density is due to this effect, with sources in the low density regime (orange data points) appearing consistently larger on average by a factor of ~ 2 than their equivalent-brightness sources in the high density regime (purple data points).

We fit a rough linear trendline to detected extended-type sources brighter than $m_r = 22.25$ mag using the `lm` linear minimisation routine (Chambers & Hastie 1992) within the R programming language (R Core Team 2020). The fit is constrained in order to accurately model the bulk population trend. We find a best fit line given by the equation $r_e = -0.15m_r + 4.25$, represented in Figure B1 as a solid bold line. Dashed lines bounding the shaded grey region represent the trend radius $\pm 25\%$. We use this relation, alongside simulated bright mock and faint missing r -band magnitudes, to estimate simulated half light radii. Simulated radii are randomly uniformly distributed within the $\pm 25\%$ boundary at a given magnitude down to an absolute minimum of 1 pixel $\pm 25\%$ (i.e., the faintest simulated source half light radii are randomly uniformly distributed in the range $[0.75, 1.25]$ pixels).

B3 Ellipticities

As with radii in Section B2, simulated ellipticities (where $e = 1 - b/a$) are likewise based upon our combined low/high density preliminary detected source catalogues. Figure B2 shows median ellipticities according to the inset colour legend in bins of half light radius along the y axis and apparent r -band magnitude along the x axis. The top panel shows our observed (detected) extended-type dataset, whilst the bottom panel shows our resultant extrapolated modelled (simulated) ellipticity dataset. Apparent magnitude data along the x axis is binned into 0.5 mag bins (see Figure 2). Half light radii are subdivided into quartiles, thereby covering the full gamut of radii within each magnitude bin. For example, median half light radii at $m_r = 21$ mag are $0.46''$ at $Q1$, $0.69''$ at $Q2$, $0.85''$ at $Q3$ and $1.04''$ at $Q4$, whilst median half light radii at the fainter $m_r = 27$ mag are $0.19''$ at $Q1$, $0.21''$ at $Q2$, $0.23''$ at $Q3$ and $0.25''$ at $Q4$. Boxes bordered by a solid black outline in the observed (detected) top panel show those bins containing 25 or fewer sources (equating to a total of 270 sources from a potential 18609), and therefore with a likely large error on the measure of ellipticity. As shown, the general trend is for larger objects to be more elliptical (less circular) at all magnitudes. Ignoring minimally occupied bins, we find a trend for detected sources becoming more circular as one progresses from bright magnitudes down to $m_r \approx 23$ mag. Continuing on to fainter magnitudes reverses this trend, with median source ellipticities becoming more elliptical once more, culminating with one of the highest overall median ellipticity bins at $m_r = 27$ mag. Following Binggeli et al. (1988), these fainter sources are increasingly likely to be morphologically irregular, in agreement with the higher ellipticities recovered here.

All observed (detected) bins containing 25 sources or more per bin (those without a surrounding solid black outline in Figure B2 in the magnitude range $21 < m_r < 27$ mag) are used to define a model fit to this feature space. Those

bins containing 25 or fewer sources exhibit a relatively large scatter on recovered median ellipticity, necessitating their exclusion here. The `lm` minimisation routine is used to fit a multi-dimensional model, with a best fit output given by:

$$\tilde{e} = 6.31564 + 0.06165 r_{e,Q} - 0.55233 m_r + 0.01217 m_r^2 \quad (\text{B1})$$

where \tilde{e} is the median ellipticity for a given bin, $r_{e,Q}$ is the half light radius quartile bin number (namely: 1, 2, 3, or 4) and m_r is the bin apparent r -band magnitude. This model is applied directly in the magnitude range $21 < m_r < 27$ mag, i.e., those magnitudes containing well-populated bins in Figure B2. To avoid extrapolation error to brighter/fainter magnitudes (e.g., Runge's phenomenon), we opt to directly map model median ellipticities from the $m_r = 21$ mag bin on to each bin in the range $m_r \leq 20.5$ mag. Similarly, we opt to directly map model median ellipticities from the $m_r = 27$ mag bin on to each bin in the range $m_r \geq 27.5$ mag. This procedure defines the model shown in the lower panel of Figure B2. Bright mock sources are assigned a simulated ellipticity given their simulated input half light radius and magnitude according to this model, with ellipticities randomly uniformly assigned in the range ± 0.2 about their modelled median ellipticity. Intermediate-brightness sources which are detected and used propagate their detected ellipticities directly. Following the trend in our faintest magnitude bin, faint missing sources are randomly uniformly assigned an ellipticity in the range 0.4 ± 0.2 .

B4 Position Angles

Associated with ellipticity is the position angle along which to align the source major axis. We opt to propagate position angles for those intermediate brightness detected and used sources directly into the simulated input catalogue. All remaining bright mock sources and faint missing sources are randomly uniformly assigned a position angle in the range $-90 < \text{P.A.} < 90$ degrees.

B5 Locations within the Field

One of the most fundamental parameters required as an input to GALSIM is at what position along x and y should the simulated source be placed. We have three varying brightness datasets: bright mock; intermediate-brightness detected and used, and; faint missing, with each requiring a different positional prescription. The simplest is for intermediate brightness detected and used source positions, which are propagated directly into the final simulated catalogue. Faint missing sources are extremely numerous, with around half a million simulated sources injected into both sample regions. Owing to their significant abundance, we opt to randomly uniformly assign faint missing source position centroids along the x axis in the range $0.5 < x < 4200.5$ pixels. Half-pixel start and end points reflect the FITS convention that the centre of the lower left corner pixel has the coordinate $[1, 1]$ and a width of 1 pixel. As with the x axis, pixel position centroids along the y axis are similarly randomly uniformly assigned in the range $0.5 < y < 4100.5$ pixels.

Determining the distribution of bright sources requires a different approach. The top two panels of Figure B3 show

arctan-scaled full-resolution images for our low density region (left) and high density region (right). As is evident, several bright sources may on occasion cluster together to form a loose group. Whether a ‘true’ group in three-dimensional space or a mere projection effect, the resulting flux bridges that link these sources on the sky leave that region prone to sky over-subtraction effects. Any investigation of this effect must therefore place bright simulated sources in such a way so as to preserve any clustering signature. We use these input images as a basis for determining such signatures. The lower two panels in Figure B3 show artificially degraded low resolution versions of their full resolution counterparts, with the low density region on the left and the high density region on the right. Each axis in the full resolution image is split into 100 ‘super pixels’, resulting in $4200/100 = 42$ super pixels along the x axis and $4100/100 = 41$ super pixels along the y axis. The mean flux value for each super pixel (equating to $42 \times 41 = 1722$ ordinary pixels) is calculated, resulting in the low resolution images shown here.

To preserve any clustering signature in our sample regions, low resolution imaging is used to define a positional weight function. A weight map is constructed by rescaling the low resolution images on to the range $[0.0 \rightarrow 1.0]$. Bright mock sources are iteratively assigned a randomly weighted position using the `sample` routine within R (Ripley 1987).

B6 Sérsic Indices

Owing to the well known bimodality in galaxy radial profiles (Baldry et al. 2004, 2006; Driver et al. 2006; Kelvin et al. 2012, 2014a,b; Taylor et al. 2015), we opt to simulate Sérsic-like galaxies with Sérsic indices of $n = 1$ (i.e., exponential disk-like) and $n = 4$ (i.e., de Vaucouleurs type spheroid-like). Each simulated region is simulated twice, with each simulated source given a Sérsic index of $n = 1$ and, separately, a Sérsic index of $n = 4$. Simulating disk-like and spheroid-like sources allows us to explore the accuracy of our sky-estimation routine as a function of source profile type, with de Vaucouleurs sources exhibiting significantly more flux in their outer wings than their exponential counterparts.

B7 Postage Stamp Cutout Sizes

Postage stamp size is the final required per-object GALSIM input parameter. Each simulated source generated by GALSIM is extrapolated out to the limits of a user-provided box, known as the postage stamp. This limitation exists for reasons of computational efficiency, notably in reducing the number of pixels requiring PSF convolution. A-priori knowledge of all relevant Sérsic parameters (magnitude, half-light radius, Sérsic index and ellipticity) allows us to determine the surface brightness drop-off as a function of semi-major axis radius for each simulated source. We opt to define postage stamp boxes for each source such that a source aligned parallel to the x -axis would reach a surface brightness limit of $\mu_r = 35 \text{ mag/arcsec}^{-2}$ at the boundary of the postage stamp. This limit is sufficiently faint to facilitate exploration of the background sky, yet not too deep to preclude the construction of these simulated frames. A mini-

um postage stamp size of 11×11 pixels is enforced²². See Section F for further discussion on the importance of choosing an appropriate postage stamp cutout size.

B8 RMS and Sky Level

To ensure that output simulated imaging exhibits Poisson noise which mimics that found in coadded sky-subtracted HSC-SSP PDR1 data, GALSIM requires as an input an estimate of the original average sky level pedestal. Unfortunately, accessing these data for this PDR1 dataset is non-trivial, with subtracted background sky maps not provided nor any easily accessible record kept of subtracted sky levels. Consequently, we calculate a basic estimate of the initial sky level based upon the root mean square (RMS) of the flux in those pixels identified as background. Given typical averaged equivalent detector gain g taken from the HSC-SSP PDR1 database and a measure of background RMS flux from our initial SOURCE EXTRACTOR runs across both density regimes, we estimate the original sky level f_{sky} in counts using the relation $f_{\text{sky}} = g \cdot \text{RMS}^2$. Using this relation, in the low density regime (8283-38) we find $\text{RMS} = 5.43 \times 10^{-2}$ counts and $f_{\text{sky}} = 1.645$ counts, whilst in the high density regime (9592-20) we find $\text{RMS} = 4.97 \times 10^{-2}$ counts and $f_{\text{sky}} = 1.391$ counts.

B9 GalSim Setup

The above sections detail the generation of all required GALSIM input parameters. With these parameters defined, input catalogues for all regions of interest are constructed. Input catalogues contain positional information alongside all other parametric variables required to construct a Sérsic model for each simulated source (see Section D for further details).

We aim to fully explore the accuracy of various background subtraction techniques as a function of field density, source profile shape and background light contamination. In addition to two density regimes (low and high as defined in Section A1, termed here as ‘denlo’ and ‘denhi’, respectively) and two profile types ($n = 1$ and $n = 4$, see Section B6), we also define a bright-end flux subset of the data. This allows us to explore the performance of sky subtraction algorithms with a known removal of faint undetected components, the primary contributors to EBL. Three simulated populations roughly segregated by flux are defined in Section B1: bright mock sources ($m_r < 22$ mag), intermediate brightness detected and used sources ($m_r > 22$ mag, becoming increasingly incomplete fainter than $m_r = 25$ mag) and faint missing sources (i.e., known missing sources in the range $m_r > 25$ mag). We define a ‘bright’ sample as the combination of those simulated sources belonging to the first two of these simulated populations, i.e., bright mock sources and intermediate brightness detected and used sources. From the initial 428257 simulated sources in the low density regime and 636215 simulated sources in the high density regime, this bright end cut extracts 6597 low density region sources and 11977 high density region sources. Taken together, we

²² This postage stamp size limit is reached only in the exponential $n = 1$ case for $\sim 12\%$ of sources.

label	based on	flux subset	source density	Sérsic index
denlo1a	8283-38	all	low	1
denlo4a	8283-38	all	low	4
denhi1a	9592-20	all	high	1
denhi4a	9592-20	all	high	4
denlo1b	8283-38	bright	low	1
denlo4b	8283-38	bright	low	4
denhi1b	9592-20	bright	high	1
denhi4b	9592-20	bright	high	4

Table B1. A summary table providing an overview of our final eight simulated regions. From left to right, columns are: dataset label; the input HSC-SSP PDR1 tract-patch ID upon which this simulated data is based; the flux population subset; the relative source density of the region; and, the Sérsic index assigned to each simulated source in that region. Flux population subset is either ‘all’ (i.e., all simulated sources as outlined in Section B1) or ‘bright’. This ‘bright’ flux subset identifier indicates that the ‘faint missing’ sources described in Section B1 are excluded from this simulation, thereby limiting it to the ‘bright mock’ and ‘intermediate detected and used’ simulated sources alone.

generate a total of eight simulated regions. These regions are summarised in Table B1.

Input catalogues for each simulated frame defined in Table B1 are constructed. An associated YAML ‘feedme’ configuration file is also generated specific to each simulated region. This configuration file specifies input and output filenames, defines the PSF and Sérsic components and assigns global parameters. For further information see Section E and Rowe et al. (2015).

B10 Simulated Fields

The GALSIM software package is run across each simulated field defined in Table B1. Figure 1 shows the results of these runs. All simulated Sérsic sources are convolved with an empirical PSF, and realistic Poisson noise has been added commensurate with typical HSC-SSP PDR1 data. The simulated background is set to zero in all of these simulations. For each density quartet (low density on the left, high density on the right) the top left panel shows the full simulated field populated exclusively with exponential $n = 1$ disk-like components. The top right panel shows the equivalent full simulated field populated exclusively with de Vaucouleurs type $n = 4$ spheroid-like components. The bottom left and bottom right panels also show the $n = 1$ and $n = 4$ fields, respectively, yet only for the bright flux sub-population as defined in Section B9 (i.e., bright mocks and intermediate brightness detected and used sources). The scale inset into the top left panel applies equivalently to all panels.

As can be seen, the absence of EBL in the lower panels marks them as visually distinct from their full simulated counterparts in the upper panels, with the background sky in the bright-only panels notably lower. Further, the extended $n = 4$ Sérsic profiles appear to visibly contaminate a relatively larger fraction of the background sky than equivalent exponential type sources do. Both such factors are potentially significant contributors to inaccurate background sky estimation.

Figure B4 shows a zoomed in region from the low density data shown in Figure 1. Here it becomes apparent that the brightest of the faint background sources present in

the full simulated data appear as faint fuzzy patches scattered across the sky. Such sources are notably missing in the bright only simulations. Their form bears a striking similarity to many such objects recorded throughout the literature, notably: the ‘small condensed galaxy’ in Arp (1965); the ‘dwarf galaxies’ of Sandage & Binggeli (1984); the ‘compact galaxies’ in Guzmán et al. (1997); the ‘little blue fuzzies’ of Brough et al. (2011); the ‘green peas’ of Cardamone et al. (2009); Bauer et al. (2013); the ‘little blue spheroids’ defined in Kelvin et al. (2014a,b); ‘low surface brightness galaxies’ in Williams et al. (2016), and; the ‘ultra diffuse galaxies’ of van der Burg et al. (2016), amongst others. Automated classification algorithms are now identifying and characterising such sources on an increasingly regular basis, as in, e.g., Sreejith et al. (2018); Turner et al. (2019), with possible formation mechanisms outlined in Stinson et al. (2007). As noted above, these systems may potentially significantly affect background sky estimation procedures.

Figure B5 shows a zoomed in region from the high density data shown in Figure 1. The zoom factor in this figure is identical to that used for Figure B4, i.e., each panel shown here shows the same solid angle on the sky as their equivalent panels in the low density regime. As noted above, the impact of faint sources is increasingly evident here. Not only do the numerous unresolved faint sources act to increase the global sky pedestal, but they also act to further enhance the wings of intermediate brightness galaxies. Such densely populated regions are becoming increasingly common in an era of low surface brightness astronomy.

The eight simulated fields summarised in Table B1 and shown in Figure 1 constitute our simulated dataset. These simulated images are background subtracted to zero counts (i.e., Poisson noise oscillates about a level of zero counts) and populated with a range of extended PSF-convolved Sérsic profile objects. These simulated data are used for all subsequent analyses throughout the remainder of this study.

APPENDIX C: THRESHOLD LEVELS

To facilitate a fair comparison of detected source catalogues generated from each of our 57 input sky-subtracted fields, we require a uniform absolute detection threshold to use as an input to SOURCE EXTRACTOR. The default operation of SOURCE EXTRACTOR identifies sources as contiguous regions of flux lying above some relative threshold level, normally 1.5σ above the locally determined sky. As sky estimation varies across fields, the resultant threshold level will also vary, therefore precluding our use of the default SOURCE EXTRACTOR configuration in this case.

To estimate a global absolute threshold level, we initially ran SOURCE EXTRACTOR in default mode on each of the 57 fields. The resultant 1.5σ threshold levels in counts are shown in the histogram in Figure C1. Individual field values are shown in the underlying rug plot. As can be seen, our threshold levels vary from ~ 0.06 counts to ~ 0.1 counts, peaking at ~ 0.07 counts. We choose this peak value of 0.07 counts as our global absolute threshold level with which to subsequently generate our source detection catalogues with the SOURCE EXTRACTOR software package.

x (pix)	y (pix)	flux (counts)	R_e (pix)	q	P.A. (deg.)	n	stamp size (pix)
527.0	2786.5	11480.40237	11.202	0.56	-38.8	1	263
387.3	454.0	7569.54847	9.987	0.55	-40.8	1	235
2460.5	1071.5	5751.59779	11.058	0.82	-1.70	1	205
1471.4	1174.9	4328.31835	7.920	0.83	39.7	1	151
4049.5	1094.9	3874.05190	8.682	0.65	-52.0	1	183

Table D1. An excerpt from the GALSIM input catalogue relating to our low density regime. This catalogue, and others of a similar format, are used by GALSIM to generate simulated imaging. Shown here are parameters relating to the five brightest simulated sources in the low density region from a total of 428257 objects. Columns, from left to right, are: x pixel position in the field; y pixel position in the field; total source flux; half light radius R_e ; axis ratio ($q = b/a$); position angle; Sérsic index n ; and, postage stamp size. Associated units (where appropriate) are shown beneath column headers in parentheses. An input catalogue of this format is generated for each simulated region.

APPENDIX D: GalSim INPUT CATALOGUES

Table D1 shows an excerpt from the input catalogue produced for the exponential ($n = 1$) simulation of the low density region. Here we show the five brightest sources out of a total of 428257 objects in this density regime. Columns, from left to right, are: x pixel position in the field; y pixel position in the field; total source flux; half light radius R_e ; axis ratio ($q = b/a$); position angle; Sérsic index n ; and, postage stamp size. Associated units (where appropriate) are shown beneath column headers in parentheses. Parameter values are rounded to a varying number of decimal places, as shown.

APPENDIX E: GalSim YAML CONFIGURATION FILES

Figure E1 shows an example YAML configuration file used as an input to GALSIM (version 2.2.6). The file is split into sections as indicated, namely, from top to bottom: global parameters; PSF information; simulated source profile setup; global image definitions; input file name; and, output processing configuration. PSF estimation and FITS file generation are detailed in Section A2. Note that the background sky level is set to zero counts in all output simulated images. Derivation of the global parameters SKYLEVEL and GAIN (an equivalent gain) are discussed in Section B8. Following initial testing, we opt to modify `kvalue_accuracy` and `maxk_threshold` from their default values to those shown here in order to minimise limiting artefacts which would otherwise be apparent in our output data. For complete definitions of these and all remaining parameters not discussed here, we refer the reader to Rowe et al. (2015).

APPENDIX F: POSTAGE STAMP SIZES

We use SOURCE EXTRACTOR to fit a single Sérsic function to each detected source as given by a prior run of either SOURCE EXTRACTOR, GNUASTRO, or the LSST PIPELINES. As an output, SOURCE EXTRACTOR provides a catalogue containing Sérsic component fitting information, and (optionally) an associated check image containing all successfully fitted Sérsic models in 2D space. Initially, we used the

SOURCE EXTRACTOR check images as the basis for our modelled masks (see Section 3.2), however, on closer inspection it became clear that these images were inappropriate for our purposes.

Figure F1 shows a comparison of SOURCE EXTRACTOR model imaging (left panels) to GALSIM model imaging (right panels) using an initial SOURCE EXTRACTOR run as the basis for determining which sources should be modelled. The top two panels show these 2D data using a standard arctan stretch, similar to figures found elsewhere in this paper. The bottom two panels show these same data using a narrower stretch, designed to highlight some of the fainter features. As is clear in the lower-left panel, SOURCE EXTRACTOR model imaging contains significant artefacts around the edges of Sérsic model sources. The default and immutable SOURCE EXTRACTOR postage stamp size is too small, resulting in a visible hard boundary at the edges of most sources. The extent of profile truncation becomes more severe as the source becomes more extended. In addition, notable edge boundary flux-wrapping artefacts are introduced for the brightest of sources, adding a peak of flux to regions where no sources were previously placed. Switching to GALSIM allows us to control the postage stamp box size used for each simulated source, resulting in a smoother and more accurate 2D modelled plane (see lower-right panel in both figures). We opt to define postage stamp boxes for each source such that a source aligned parallel to the x -axis would reach a surface brightness limit of $\mu_r = 35 \text{ mag/arcsec}^{-2}$ at the boundary of the postage stamp. This limit was chosen to be sufficiently faint to facilitate exploration of the background sky, yet not too deep to become overly computationally expensive. A minimum postage stamp size of 11×11 pixels is enforced at all times.

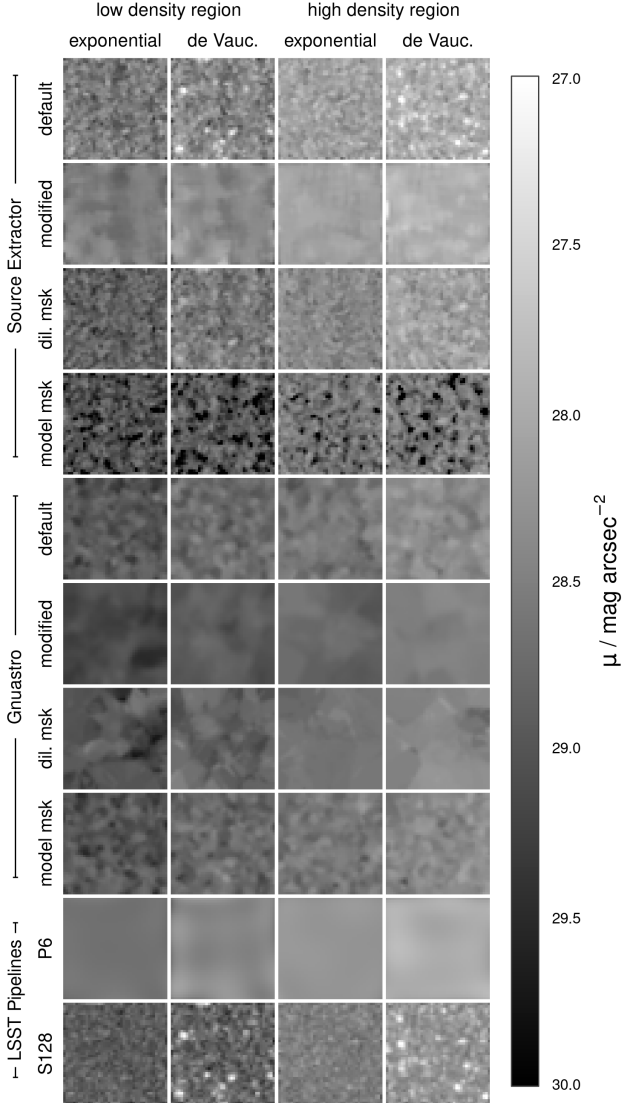


Figure 6. Recovered background sky maps generated by various sky estimation and source extraction configurations. Rows depict different software configuration modes. Columns represent the recovered background sky maps generated from different input simulated datasets. Each original 4200×4100 pixel image has been mean-binned into 100×100 pixel super-pixels and colour-coded according to its mean surface brightness value, as shown by the outlying colour bar. High density simulated regions are brighter than their low density counterparts by $\Delta\mu_{\text{hi-lo}} = -0.43 \text{ mag arcsec}^{-2}$ on average, owing to the greater number of contaminant sources littering the field. Similarly, simulated regions populated with extended de Vaucouleurs sources are brighter than their exponential source equivalents by $\Delta\mu_{4-1} = -0.21 \text{ mag arcsec}^{-2}$ on average. Note how some sky estimation software configuration modes also recover a background sky with relatively fewer spatial fluctuations, an indicator that those particular configurations are less impacted by singular bright sources.

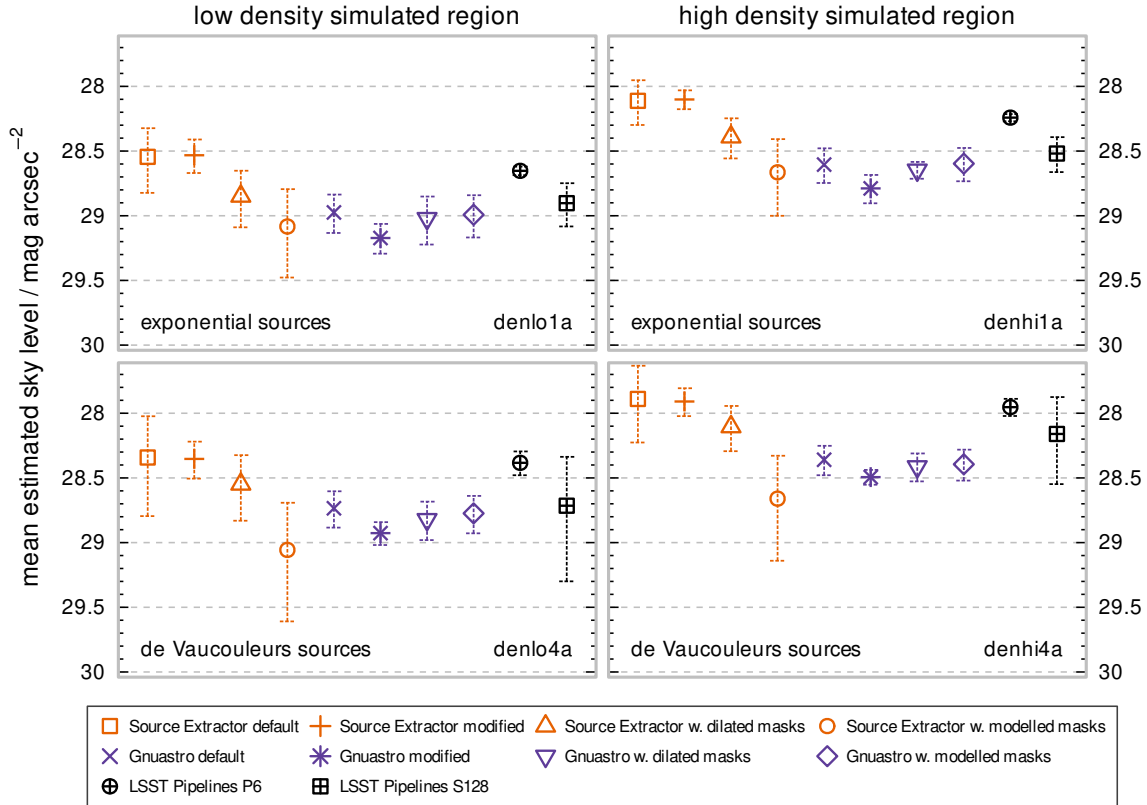


Figure 7. Mean estimated sky levels recovered for our complete simulated data as generated by SOURCE EXTRACTOR (orange), GNUASTRO (purple) and the LSST PIPELINES (black) operating in various configurations (shown within the legend). Distinct software configuration modes are equally spaced along the x-axis within each panel, for clarity. The uppermost two panels represent simulated regions consisting of exponential ($n = 1$) sources alone. The lower two panels represent simulated data consisting of de Vaucouleurs ($n = 4$) sources alone. The left side panels represent low density simulated regions, whilst the right side panels represent high density simulated regions. Specific simulation data IDs are inset within each panel (see Table B1). Error bars represent $\pm 1\sigma$ about the mean. The impact of source density and source profile shape on the resultant sky level estimates shown here is evident, with higher density and extended source types (i.e., denhi4a) consistently brighter by up to an order of magnitude than that of their lower density or less extended simulated imaging counterparts. Various software configurations appear to consistently outperform others, with the discrepancy between the best and worst performing configurations similarly spanning half a magnitude. The shape of sky level offsets between configurations appears relatively static as a function of field type, only varying in the overall amplitude.

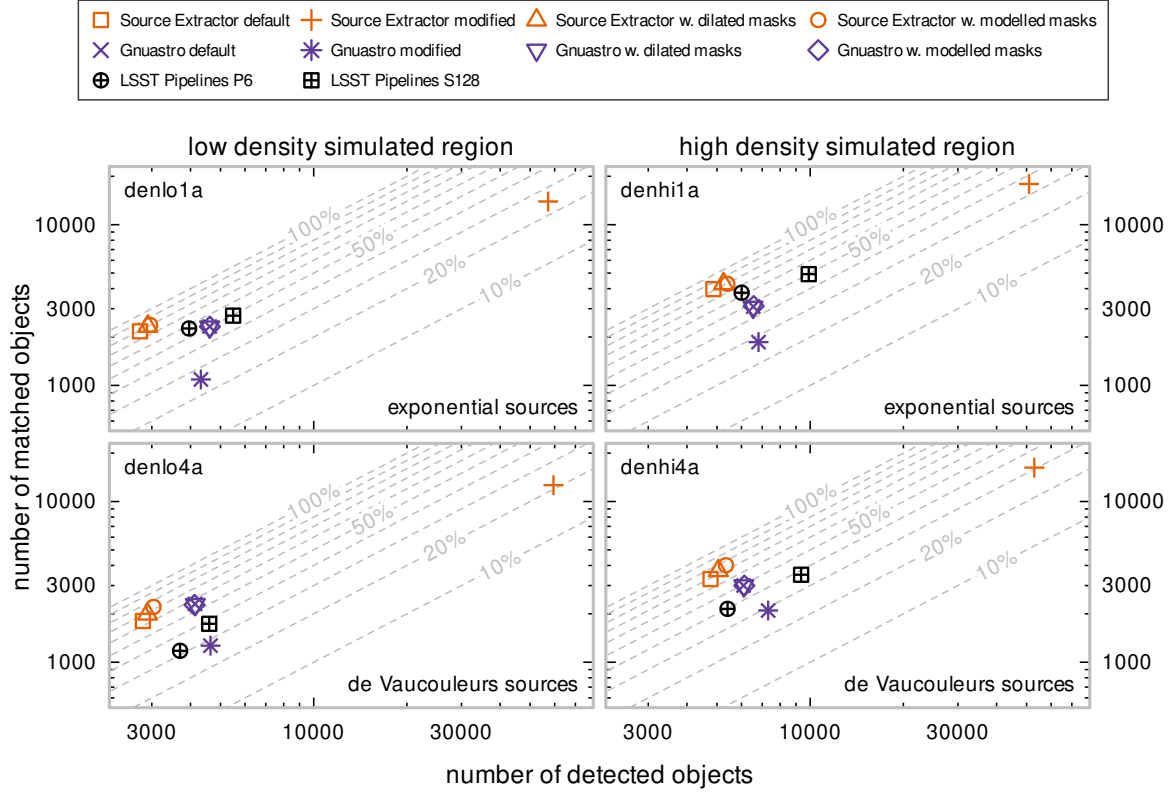


Figure 8. Number of true matched objects as a function of the total number of detected objects given by the various sky estimation and source extraction software configuration modes listed in the legend. Output sources are matched to their corresponding simulated input counterpart if they satisfy three criteria: the x and y output pixel positions fall within 5 pixels of the input source, and the recovered magnitude is within ± 0.5 mag of its input total magnitude. Dashed grey lines represent matched-to-total ratios in 10% increments. The SOURCE EXTRACTOR outputs typically return the highest fidelity ratios, with GNUASTRO and the LSST PIPELINES instead leaning towards recovery of more objects.

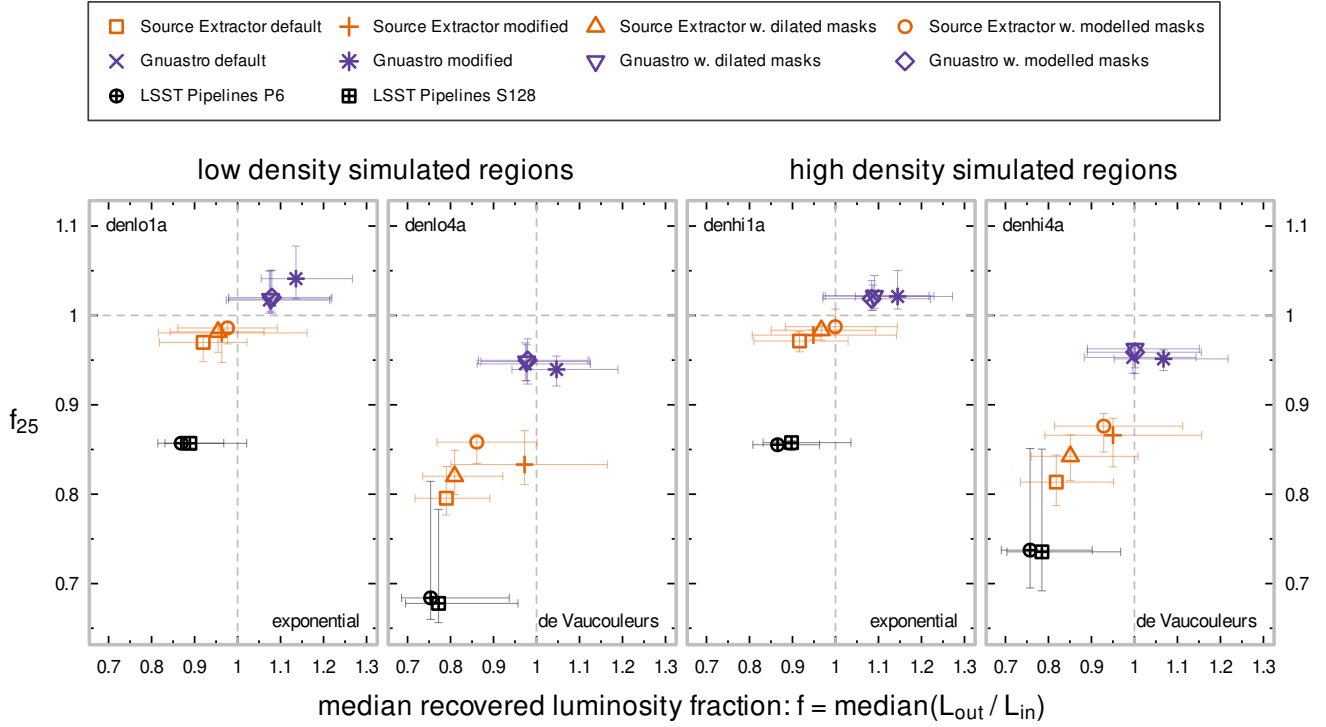


Figure 9. Median recovered luminosity fractions (output/input) for matched sources as determined by various source extraction techniques listed in the accompanying legend. Each panel represents a different simulated input dataset flavour, as indicated by the supporting label text. Within each panel, the x -axis represents the median recovered luminosity fraction f for all matched sources, where $f = \text{median}(L_{\text{out}}/L_{\text{in}})$, whilst the y -axis represents the median recovered luminosity fraction for the 25 largest sources alone (f_{25} , i.e., those sources that have the largest impact on background sky estimation and are equivalently most severely impacted by it). Error bars represent 25th and 75th percentile ranges. These results show that SOURCE EXTRACTOR performs well with exponential type sources, accurately recovering close to 100% of the simulated input flux, whilst under-estimating total flux for the more extended de Vaucouleurs type sources by $\sim 15\%$, as expected. Conversely, GNUASTRO performs well for the majority of de Vaucouleurs types, missing $\sim \text{few}\%$ of the flux for the largest de Vaucouleurs type sources, however, incorrectly over-estimating flux for exponential type sources by $\sim 10\%$, and always over-estimating flux when run its modified configuration mode.

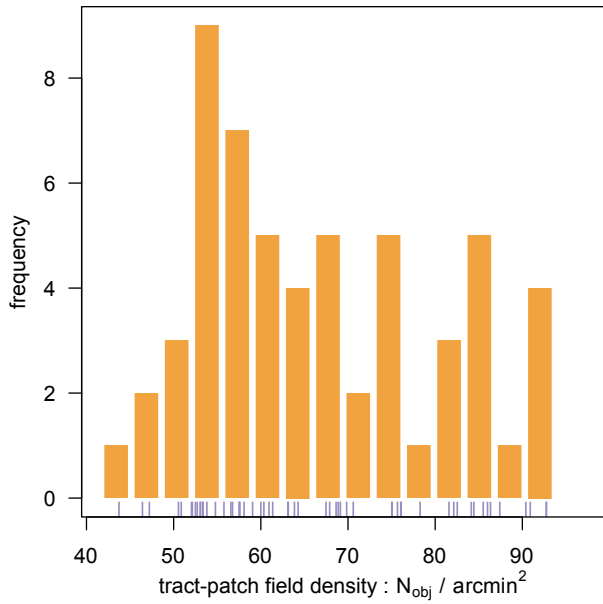


Figure A1. Initial estimate of field density for all 57 tract-patch regions using a constant absolute detection threshold of 0.07 counts. Each patch is approximately 0.196 deg on a side. Using these data, we select the tract-patch fields located at the 5th and 95th percentiles of recovered field density to respectively represent our low-density and high-density input observed datasets.

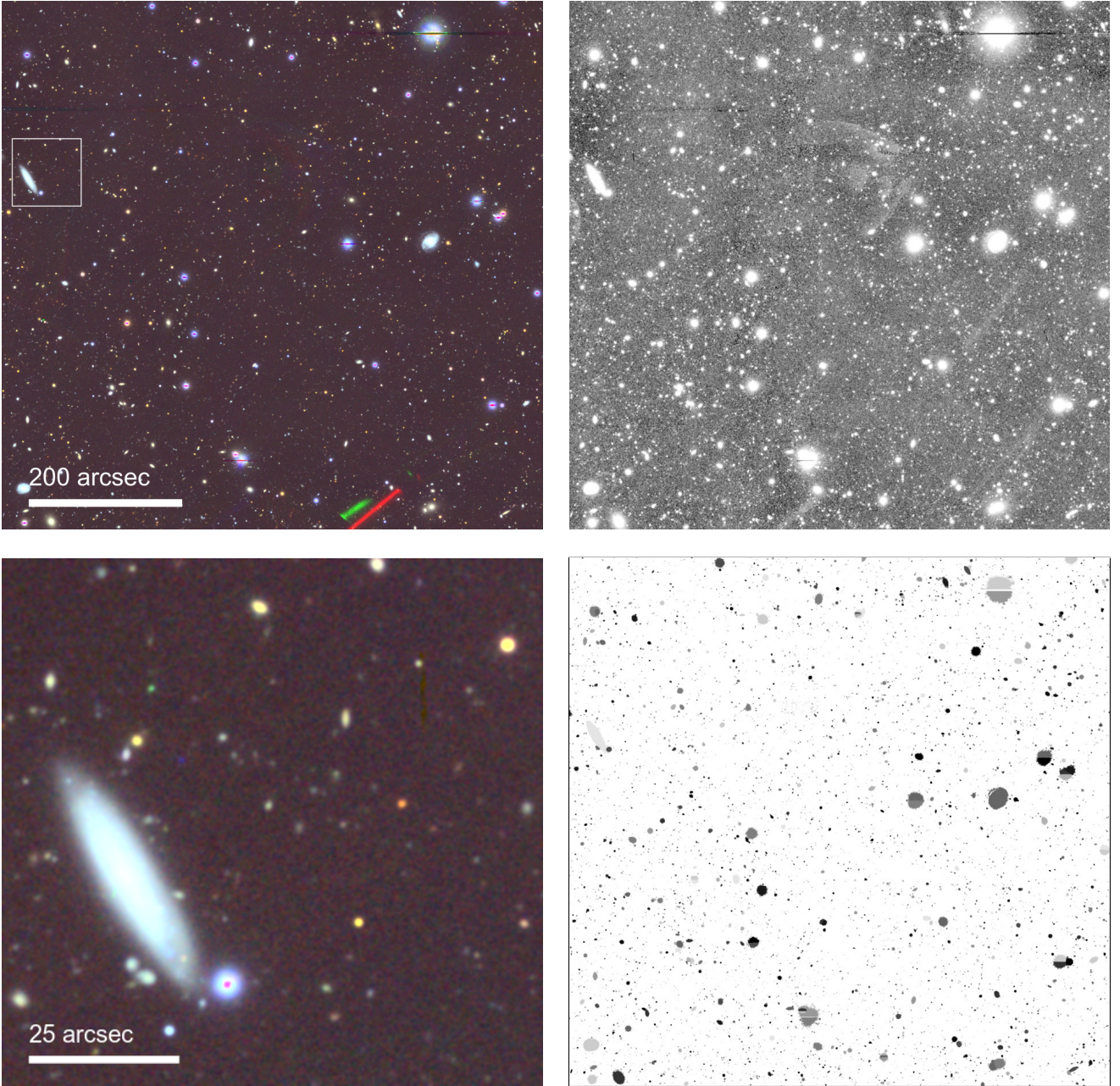


Figure A2. HSC-SSP PDR1 low density region, tract-patch 8283-38. Clockwise from top left: RGB postage stamp of the entire 706×689 arcsec region; r -band postage stamp; segmentation map; and RGB postage stamp for a 90×88 arcsec zoomed cutout. All postage stamps are arctan scaled and smoothed with a Gaussian kernel of $\Gamma = 3$ pix. RGB images are generated using HSC-SSP z , i and r passbands. The white box in the upper-left panel shows the zoomed in region displayed in the lower-left panel. Shades of grey within the segmentation map are randomly assigned. This low-density region will be used as a basis for the generation of a low-density simulated field.

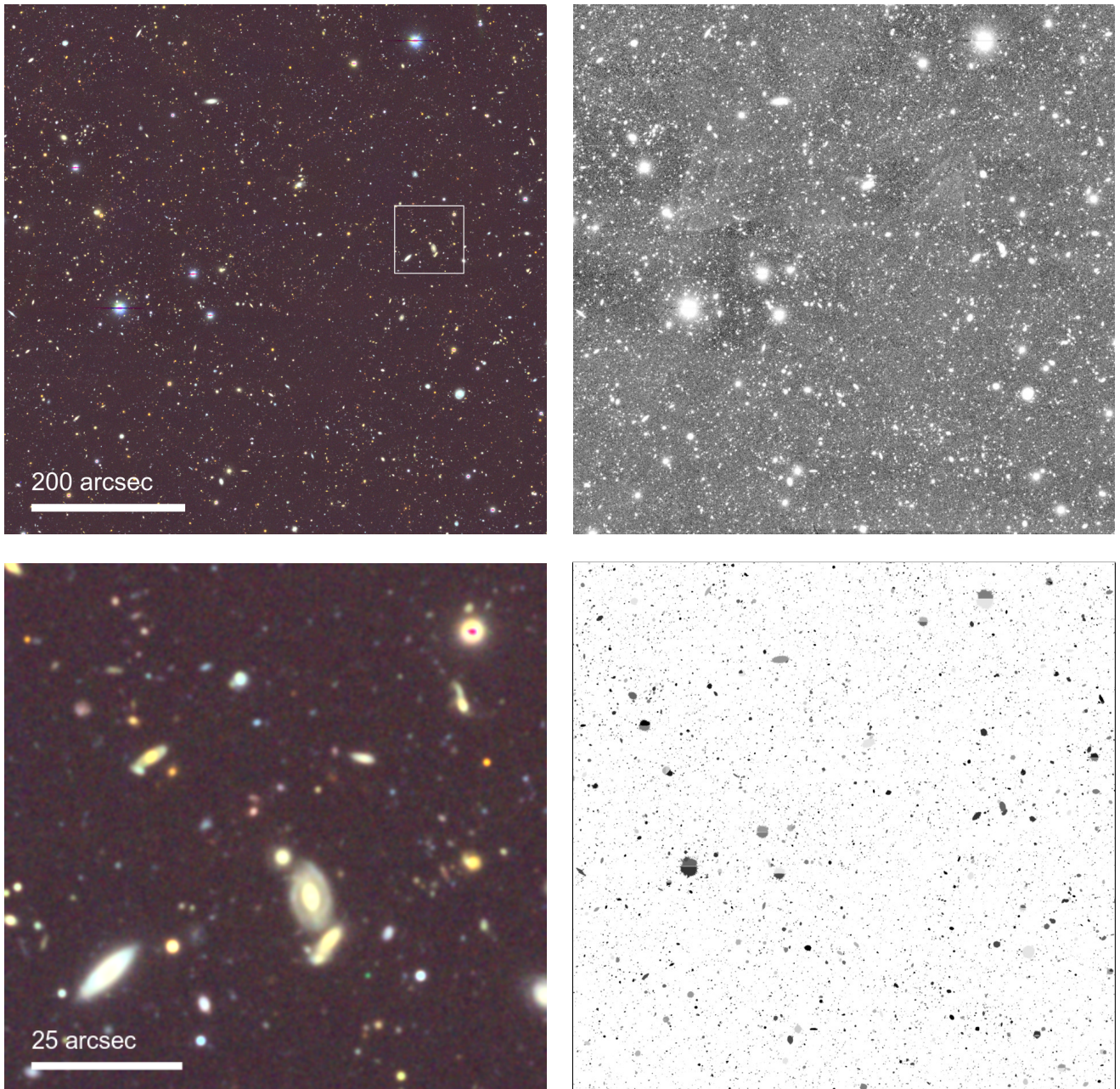


Figure A3. As Figure A2, but for the HSC-SSP PDR1 high density region, tract-patch 9592-20.

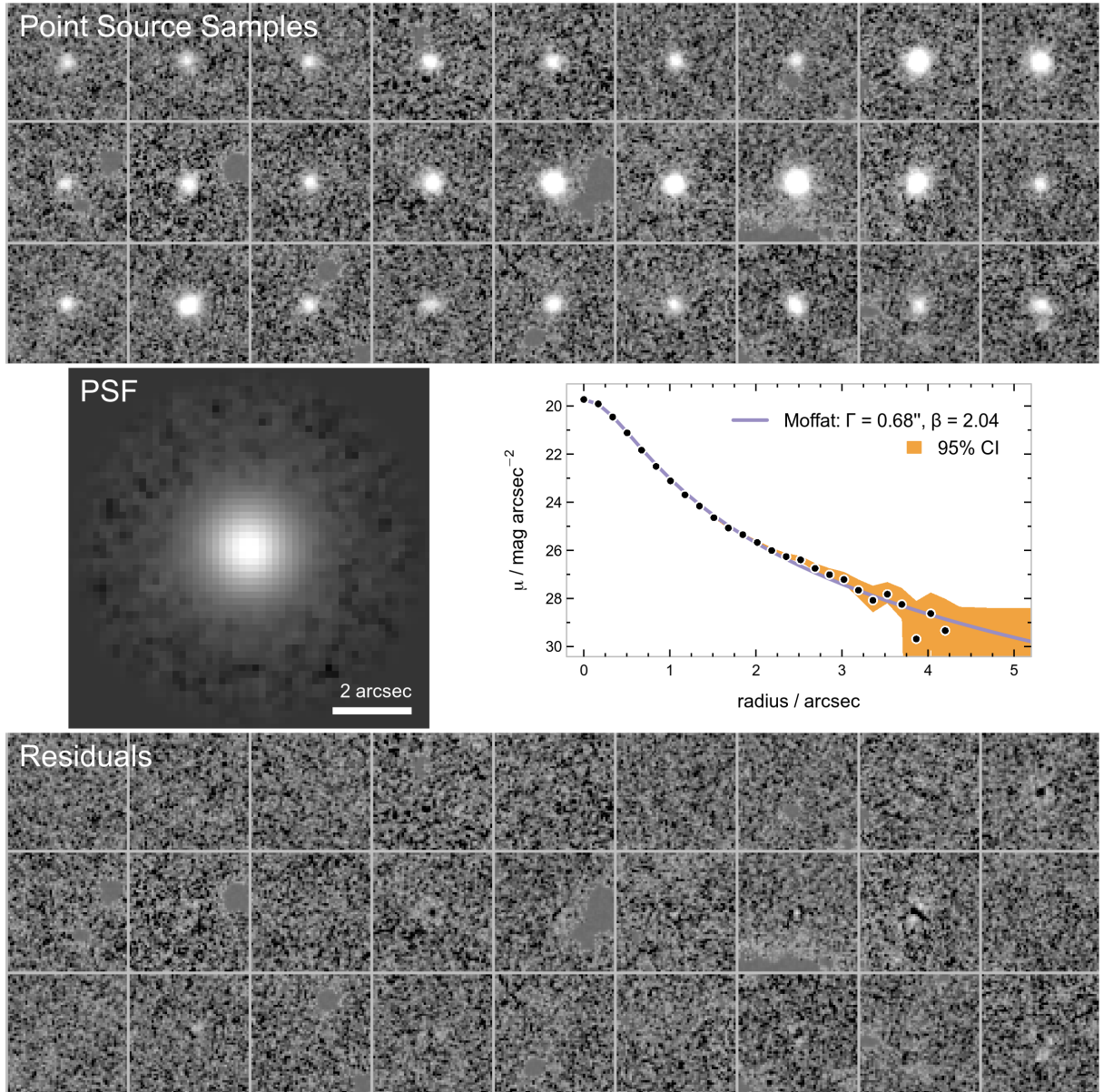


Figure A4. Visualisation of key outputs from the PSFEX PSF modelling software, as applied to our HSC-SSP PDR1 low-density dataset (tract-patch 8283-38). Top: 27 sample point sources, arcsinh scaled, from a total of 424 used as an input to the PSF generation software. Middle-left: empirical PSF, log scaled, generated as the output of an 2^{nd} -order polynomial fit to the shape and position of all sample point sources. Middle-right: 1D surface brightness profile of the PSF, showing the PSF data (black points), 95% confidence interval (shaded orange region), and a Moffat profile fit to the observed data (purple line). Fitted Moffat parameters are shown in the inset legend. Bottom: PSF residual images, arcsinh scaled, representing the results of a flux-scaled PSF subtraction from each point source in the top panel. Much of the point source flux has been successfully removed in the residual frames, evidencing the high-fidelity nature of the output PSF model.

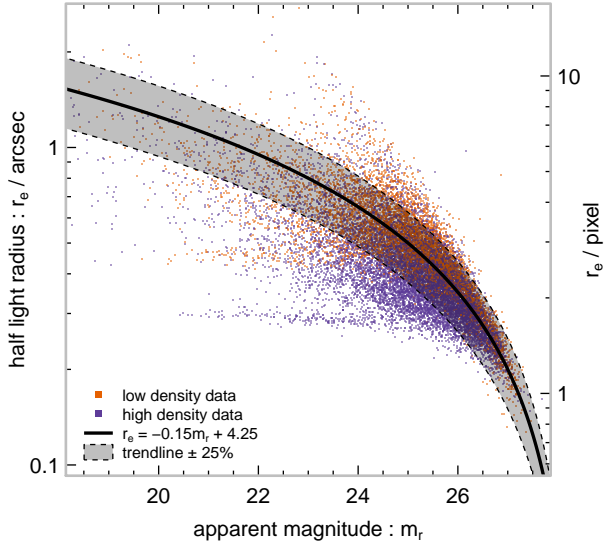


Figure B1. Recovered half-light radii as a function of apparent r -band magnitude for all extended-type ($\text{CLASS_STAR} < 0.05$) detected sources. Sources from the low density region are shown in orange, whilst sources from the high density region are shown in purple. The solid bold black line represents a best fit trendline to those extended-type sources brighter than $m_r = 22.25$ mag. Simulated bright mock and faint missing sources are randomly distributed within the $\pm 25\%$ boundaries about this trendline down to an absolute minimum of 1 pixel.

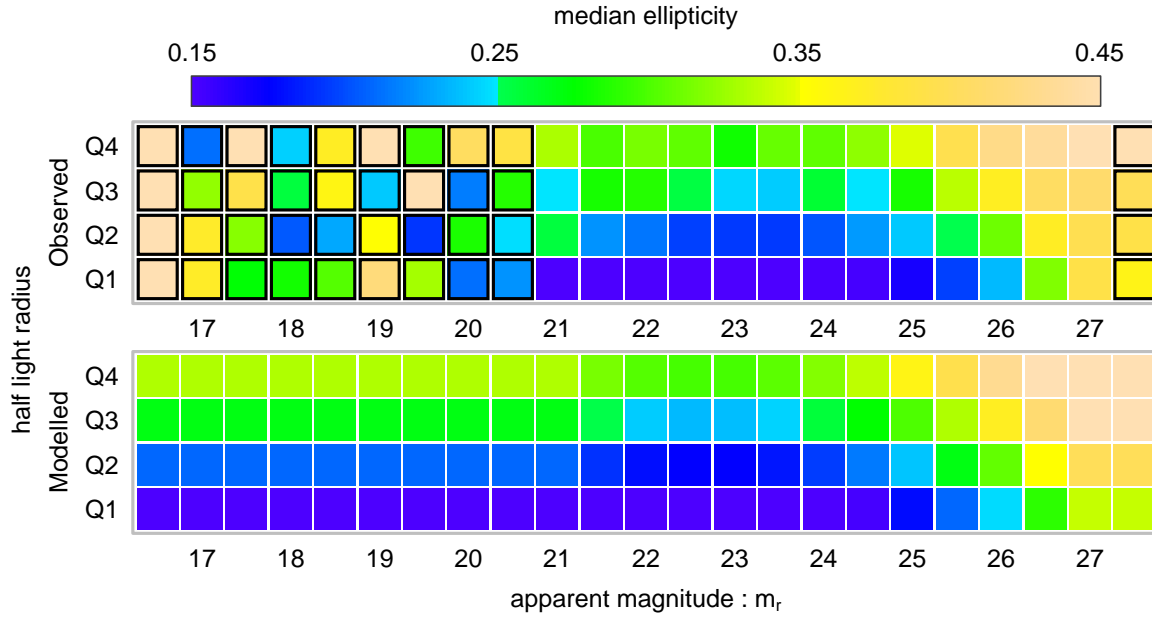


Figure B2. Median ellipticities in bins of half light radius and apparent r -band magnitude. Observed (detected) extended-type data is shown in the top panel, modelled (simulated) data is shown in the bottom panel. Observed bins enclosed within a solid black border represent minimally occupied bins containing 25 or fewer sources. A fit to all remaining bins with 25 or more sources each is used to construct the model in the lower panel (see text for more details).

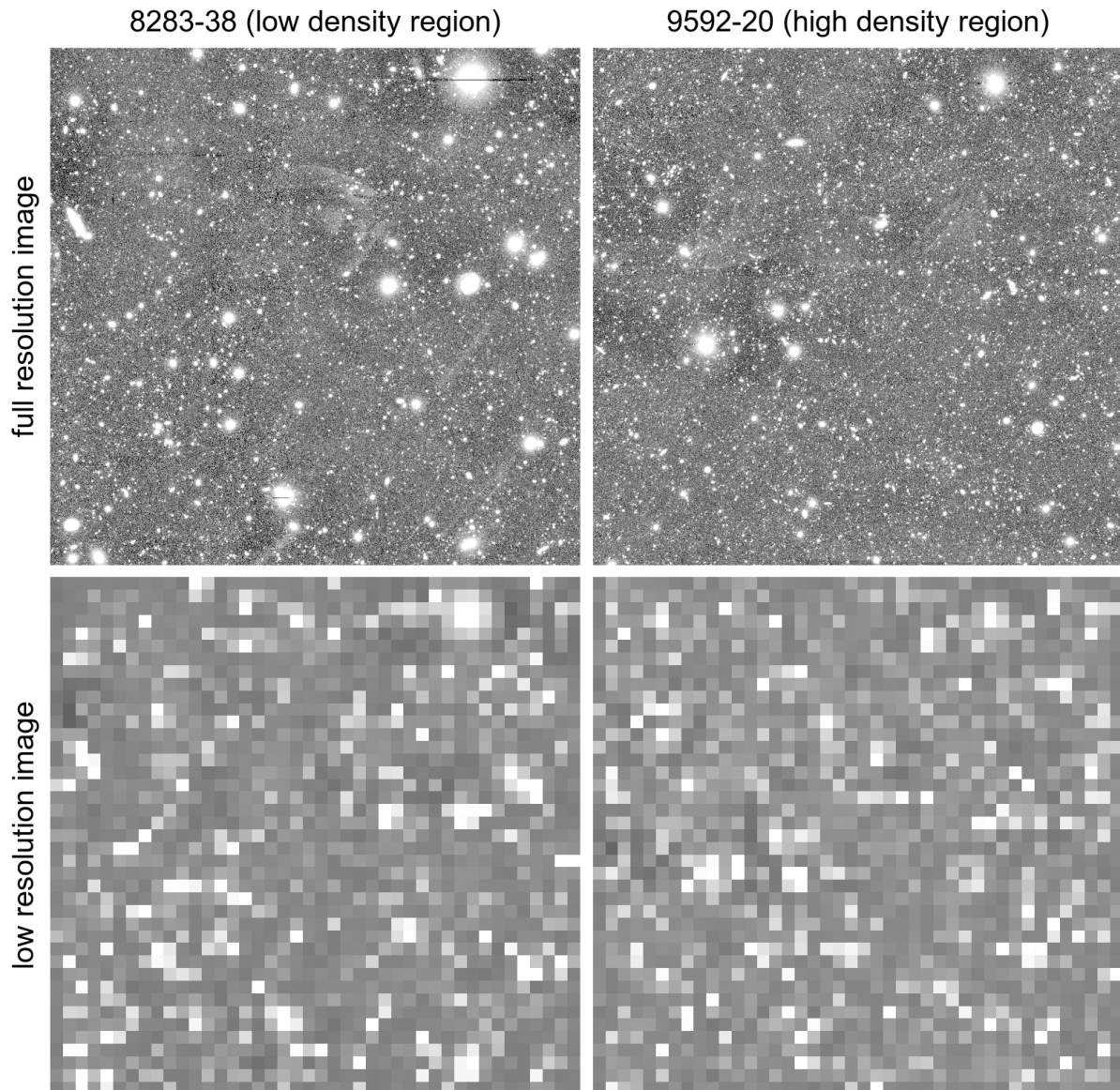


Figure B3. HSC-SSP PDR1 full-resolution (top) and artificially degraded low-resolution (bottom) imaging for both sample regions: low density on the left and high density on the right. Images are arctan scaled. Full resolution images are smoothed with a Gaussian kernel of $\Gamma = 3$ pix prior to plotting. Each super pixel in the low resolution image is a mean of $42 \times 41 = 1722$ ordinary pixels in the original data. Low resolution images are used to define a weight function when determining bright mock source centroid placement.

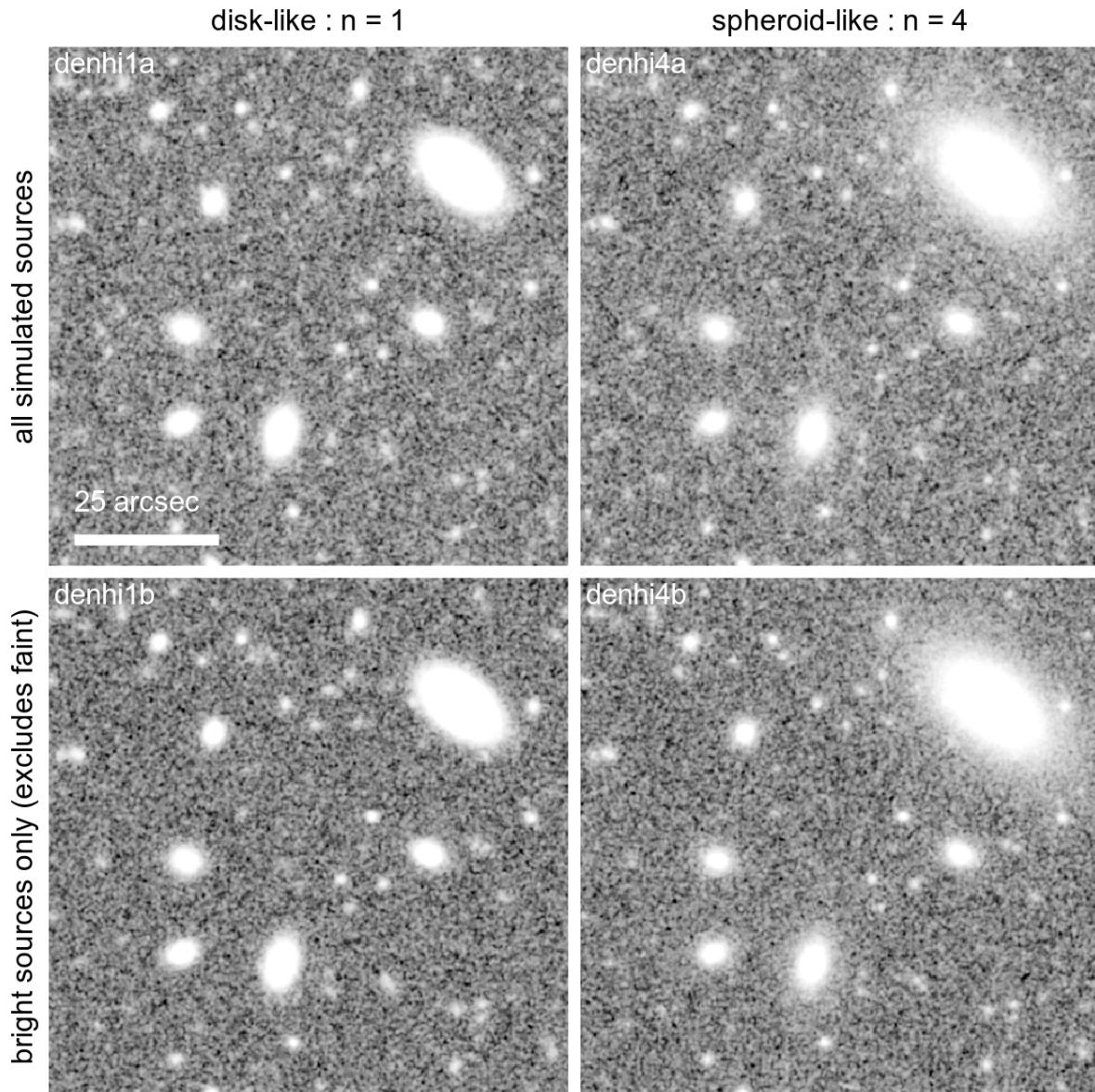


Figure B4. Low density simulated fields. As for the low density data shown in Figure 1, but for a zoomed in region as represented by the inset scale. When zoomed in, the presence (top row) or otherwise (bottom row) of faint EBL sources and their impact on the apparent sky level is visibly evident.

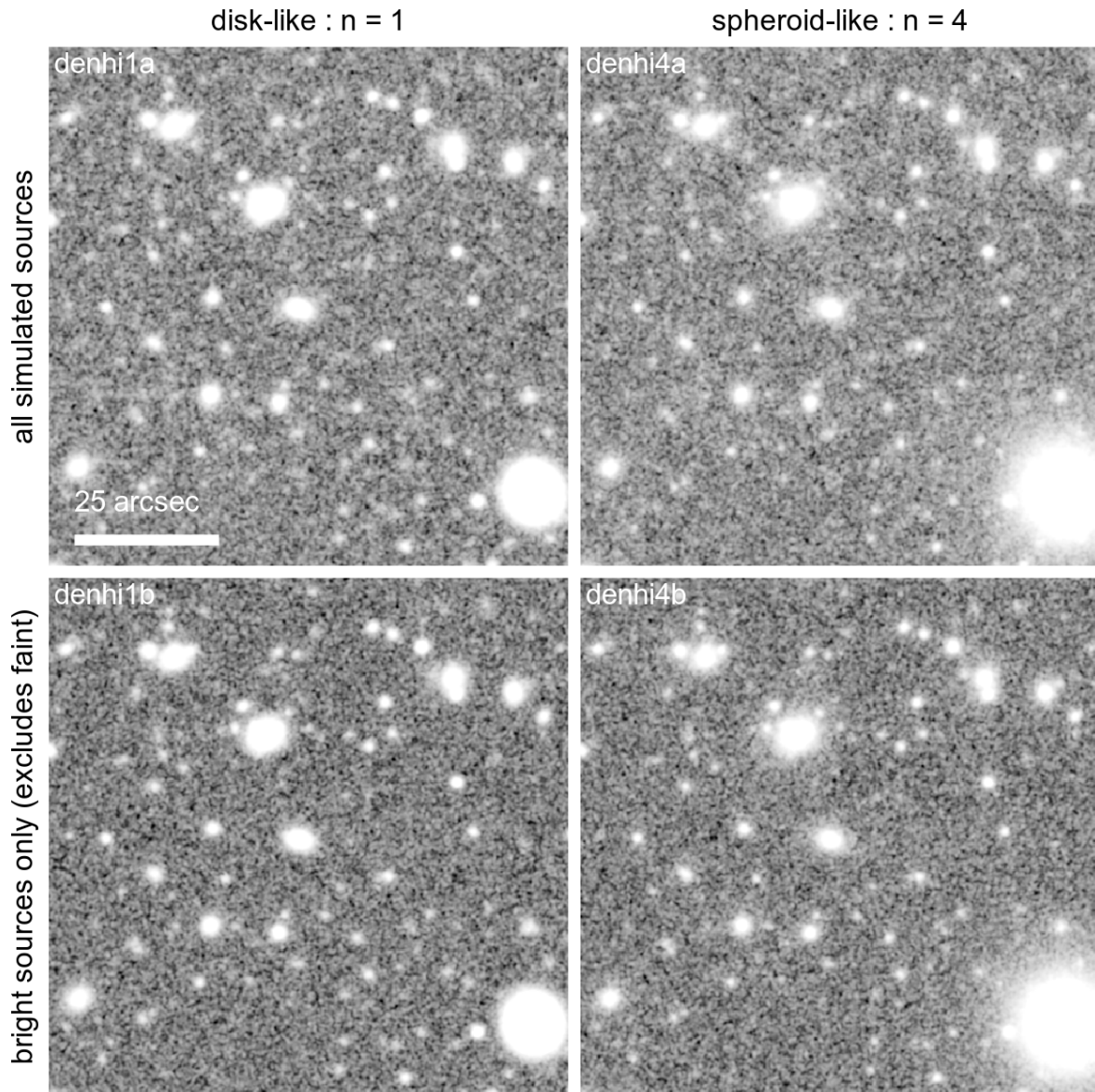


Figure B5. High density simulated fields. As for the high density data shown in Figure 1, but for a zoomed in region as represented by the inset scale. As with the low density region, when zoomed in, the presence or otherwise of faint EBL sources and their impact on the apparent sky level is visibly evident.

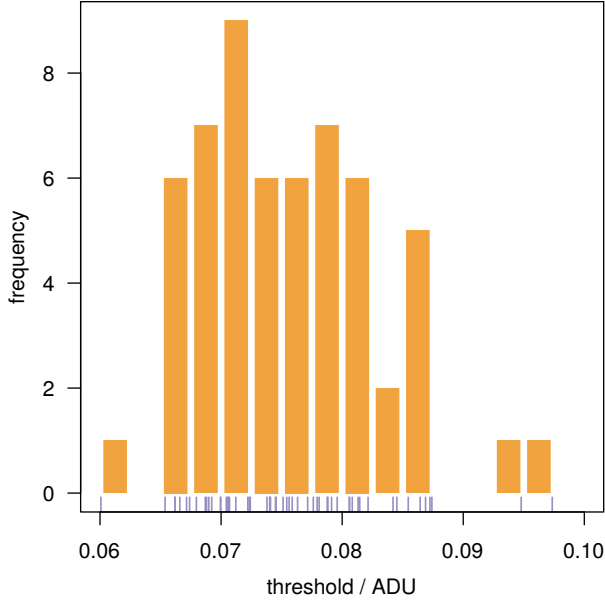


Figure C1. Histogram showing relative 1.5σ detection threshold levels as output by SOURCE EXTRACTOR when operated in default mode upon each of our 57 input fields. Individual field values are shown in the underlying rug plot. We adopt a threshold level of 0.07 counts as our global absolute detection threshold level, corresponding to the approximate position of the peak in this figure.

```

parameters :
- &output output.fits
- &input input.dat
- &sky_level_pixel SKYLEVEL
- &gain GAIN
- &pixelscale 0.168

psf :
type : InterpolatedImage
image : "psf.fits"
scale : *pixelscale

gal :
type : Sersic
n : { type : Catalog , col : 6 }
half_light_radius :
type : Eval
fpixelscale : *pixelscale
fhlrpixel : { type : Catalog , col : 3 }
str : 'hlrpixel * pixelscale'
flux : { type : Catalog , col : 2 }
ellip :
type : QBeta
q : { type : Catalog , col : 4 }
beta :
type : Degrees
theta : { type : Catalog , col : 5 }

gsparams:
kvalue_accuracy : 1.e-8
maxk_threshold : 1.1e-4

image :
pixel_scale : *pixelscale
sky_level : 0 # ADU / arcsec^2
random_seed : 3125
nproc : 3
type : Scattered
xsize : 4200 # pixel
ysize : 4100 # pixel
stamp_size : { type : Catalog , col : 7 } # pixel
image_pos :
type : XY
x : { type : Catalog , col : 0 }
y : { type : Catalog , col : 1 }
noise :
type : CCD
sky_level_pixel : *sky_level_pixel # ADU/pixel
gain : *gain # e-/ADU
read_noise : 0 # ADU

input :
catalog :
file_name : *input

output :
file_name : *output
nproc : 3
type : Fits

```

Figure E1. An example YAML configuration file used as an input to GALSIM. This configuration file produces a simulated output.fits file based on the input.dat input catalogue. PSF generation is outlined in Section A2, whilst estimates of the original sky level pedestal (SKYLEVEL) and averaged detector equivalent gain (GAIN) are detailed in Section B8. See the text for further information.

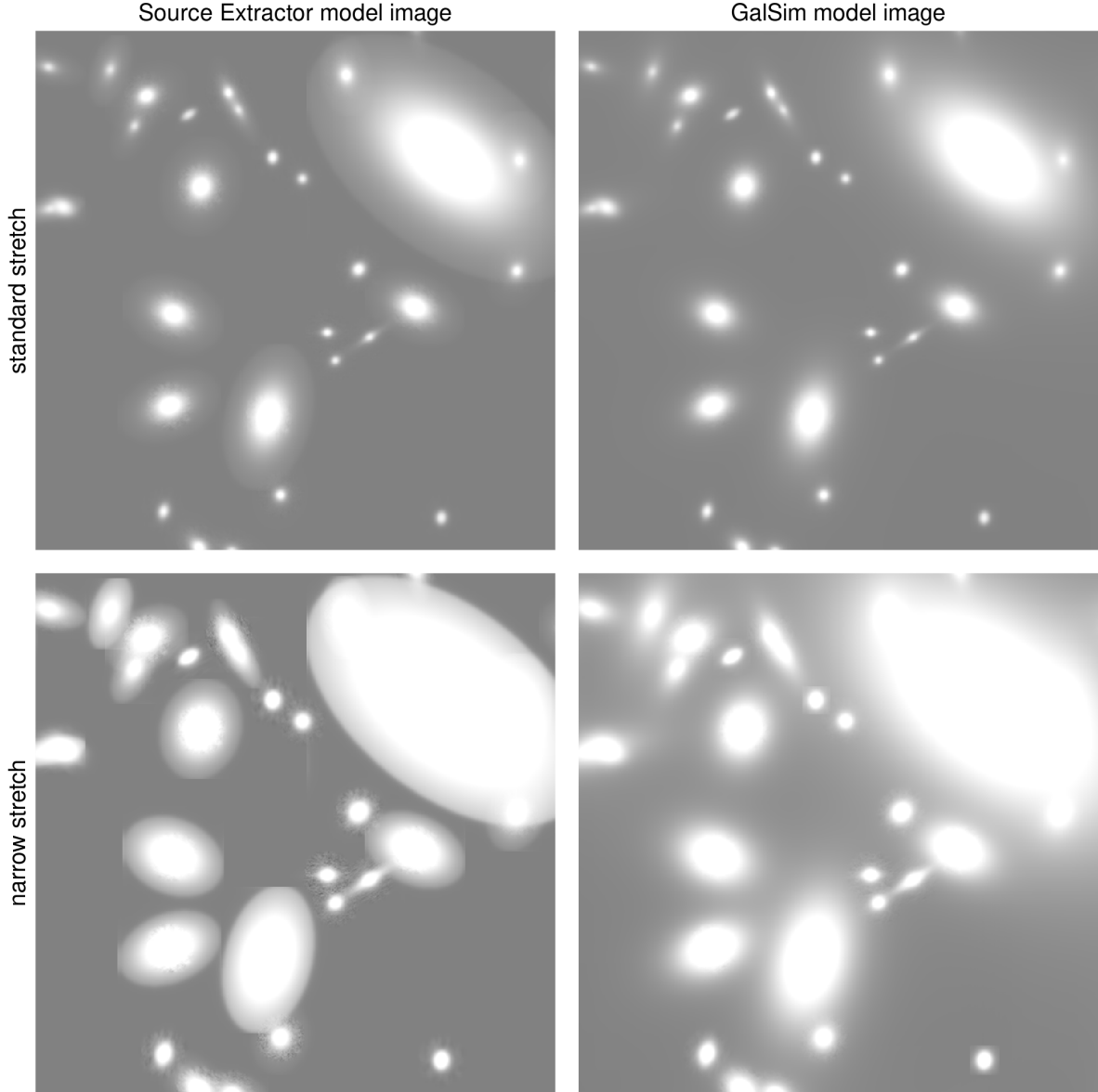


Figure F1. A comparison of initial Sérsic model imaging produced by SOURCE EXTRACTOR (left panels) to our final utilised refined GALSIM Sérsic modelled imaging (right panels). Model Sérsic parameters are derived from SOURCE EXTRACTOR. The upper two panels show model imaging using a standard arctan z -scale stretch, similar to that found elsewhere in this paper. The lower two panels are arctan scaled over a narrower z -scale stretch, highlighting LSB flux around the outskirts of sources. Whilst SOURCE EXTRACTOR seemingly produces robust Sérsic catalogue data, it does not allow the user to control the postage stamp size out to which Sérsic models are propagated in an accompanying check image. As a result, various modelled source edge effects are visible (see left panels) in output SOURCE EXTRACTOR check imaging owing to the fact that the default SOURCE EXTRACTOR postage stamp size is too small for the purposes of this study. We use GALSIM to define bespoke postage stamps for each simulated source (see right panels), minimising this effect.